East Asian Journal on Applied Mathematics
doi: 10.4208/eajam.2025-007.190525

Vol. **xx**, No. x, pp. 1-28
xxx 2025

High-Order BDFk Parametric Finite Element Methods for Anisotropic Surface Diffusion Flows and Applications in Solid-State Dewetting

Lechuan Gu, Yihang Guo and Meng Li*

School of Mathematics and Statistics, Zhengzhou University, Zhengzhou 450001, China.

Received 11 January 2025; Accepted (in revised version) 19 May 2025.

Abstract. In this paper, we extend the BGN formulation [J.W. Barrett, H. Garcke and R. Nürnberg, J. Comput. Phys. 222 (2007)] by incorporating the k-order backward differentiation formulae (BDFk) for time discretization. This allows us to develop high-order temporal parametric finite element methods for simulating anisotropic surface diffusion flows and solid-state dewetting problems, achieving accuracy levels from second-order to fourth-order. We prove the well-posedness of the constructed high-order schemes. The proposed schemes maintain good mesh quality characteristic of the classical first-order BGN scheme. Finally, we present several numerical simulations to demonstrate the high-order temporal accuracy and verify the preservation of good mesh quality and energy stability throughout the evolution.

AMS subject classifications: 65M60, 65M12, 53C44, 35K55

Key words: Parametric finite element method, BGN scheme, BDFk, high-order accuracy, energy stability.

1. Introduction

Surface diffusion refers to the movement of atoms, ions, molecules, and atomic clusters along the surface of a solid. The anisotropy of solid materials, characterized by varying periodicity and density of atomic arrangements in different lattice directions, leads to direction-dependent physical and chemical properties. This intrinsic anisotropy gives rise to anisotropic surface energy, which in turn governs anisotropic surface diffusion on solid surfaces [44]. Anisotropic surface diffusion is crucial in various applications across materials science and physics, including the evolution of voids in microelectronic circuits [41], microstructural evolution in solids [13,22], and solid-state dewetting (SSD) [26,36,39,40,45,46,50], among others.

*Corresponding author. *Email addresses:* gulechuanzzu@outlook.com (L. Gu), 15836578103@163.com (Y. Guo), limeng@zzu.edu.cn (M. Li)

Let $\Gamma = \Gamma(t)$ be a two-dimensional closed curve represented as

$$\vec{X} := \vec{X}(s,t) = \big(x(s,t), y(s,t)\big)^T,$$

where s is the arc-length parametrization of Γ and t denotes time — cf. Fig. 1. Besides, let $\vec{n} = (n_1, n_2)^T \in \mathbb{S}^1$ be the outward unit normal vector, $\gamma = \gamma(\vec{n})$ a given anisotropic surface energy, and $\vec{\tau} = \partial_s \vec{X} = \vec{n}^{\perp}$, $\vec{n} = -\partial_s \vec{X}^{\perp} = -\vec{\tau}^{\perp}$, where $\perp$ denotes the clockwise rotation by angle $\pi/2$.

We consider a homogeneous extension $\gamma(\vec{p}) : \mathbb{R}^2_* := \mathbb{R}^2 \setminus \{\vec{0}\} \to \mathbb{R}^+$ of the anisotropic surface energy $\gamma(\vec{n}) : \mathbb{S}^1 \to \mathbb{R}^+$ such that:

(i) $\gamma(\vec{p})|_{\vec{p}=\vec{n}} = \gamma(\vec{n})$ for $\vec{n} \in \mathbb{S}^1$.

(ii) $\gamma(c\vec{p}) = c\gamma(\vec{p})$ for $c > 0$ and $\vec{p} \in \mathbb{R}^2_*$.

One of popular homogeneous extensions is

$$\gamma(\vec{p}) := |\vec{p}|\gamma\left(\frac{\vec{p}}{|\vec{p}|}\right) \quad \text{for all} \quad \vec{p} = (p_1, p_2)^T \in \mathbb{R}^2_* := \mathbb{R}^2 \setminus \{\vec{0}\},$$
$$\gamma(\vec{p}) := 0, \vec{p} = \vec{0},$$

where $|\vec{p}| = \sqrt{p_1^2 + p_2^2}$, cf. Refs. [2, 15, 29].

The following geometric evolution equation

$$\partial_t \vec{X} = \partial_{ss} \mu \vec{n}, \tag{1.1}$$

where $\mu := \mu(s)$ is the chemical potential, characterizes the motion of the curve driven by anisotropic surface diffusion [14, 40, 42]. The Cahn-Hoffman $\vec{\xi}$-vector [23, 47], the

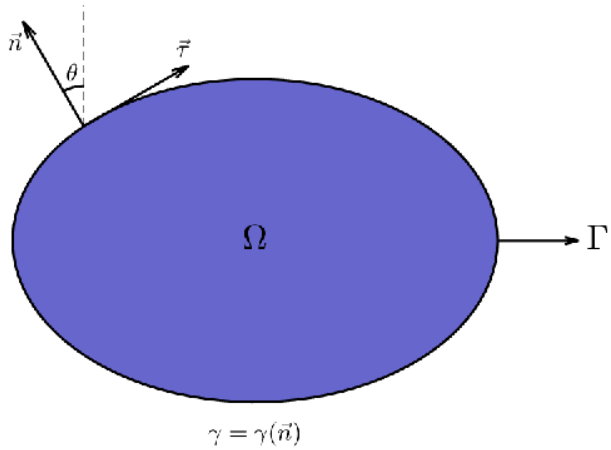

Figure 1: Schematic diagram of a closed curve Γ under anisotropic surface diffusion. The anisotropic surface energy is $\gamma(\vec{n})$, while $\vec{n}$ is the outward unit normal vector.

chemical potential μ and the Hessian matrix $\mathbf{H}_\gamma(\vec{n})$ [29] can be defined by

$$\begin{aligned}
&\vec{\xi} := \vec{\xi}(\vec{n}) = \nabla\gamma(\vec{p})\big|_{\vec{p}=\vec{n}} = \gamma(\vec{n})\vec{n} + (\vec{\xi}\cdot\vec{\tau})\vec{\tau} \quad \text{for all} \quad \vec{n}\in\mathbb{S}^1,\\
&\mu := -\vec{n}\cdot\partial_s\vec{\xi}^{\perp},\\
&\mathbf{H}_\gamma(\vec{n}) := \nabla\nabla\gamma(\vec{p})\big|_{\vec{p}=\vec{n}}.
\end{aligned} \tag{1.2}$$

It follows from (1.1) and (1.2) that the anisotropic surface diffusion flow (SDF) for Γ can be represented as

$$\begin{aligned}
&\partial_t\vec{X} = \partial_{ss}\mu\,\vec{n}, \quad 0<s<L(t), \quad t>0,\\
&\mu = -\vec{n}\cdot\partial_s\vec{\xi}^{\perp}, \quad \vec{\xi} = \nabla\gamma(\vec{p})\big|_{\vec{p}=\vec{n}},
\end{aligned} \tag{1.3}$$

where $L(t)=\int_{\Gamma(t)} ds$ is the length of $\Gamma(t)$, cf. [2,29]. The initial condition for (1.3) is given by

$$\vec{X}(s,0) = \vec{X}_0(s) = \big(x_0(s), y_0(s)\big)^T, \quad 0\le s\le L_0, \tag{1.4}$$

where L_0 represents the length of the initial curve.

There are various numerical methods used in simulation of isotropic and anisotropic surface diffusion, including the finite element method (FEM) with graph representations [1,15,16], the level set and phase-field methods [19], the discontinuous Galerkin FEM [49], the marker-particle method [18,48], the θ-L formulation method [25], and the parametric FEM (PFEM) [2,9,11,29,37,40]. Note that the methods proposed by Barrett *et al.* [8,9,12], collectively referred to as BGN, stand out because of their unconditional energy stability and adaptability to asymptotic mesh distributions. Following the concept of BGN methods, the SDF (1.3) is reformulated as

$$\begin{aligned}
&\vec{n}\cdot\partial_t\vec{X} = \partial_{ss}\mu, \quad 0<s<L(t), \quad t>0,\\
&\mu\vec{n} = -\partial_s\vec{\xi}^{\perp}, \quad \vec{\xi} = \nabla\gamma(\vec{p})\big|_{\vec{p}=\vec{n}}.
\end{aligned}$$

The BGN method improves mesh quality without using mesh retriangulation techniques. Instead, it introduces the artificial tangential velocity, effectively handling the problem of node clustering and mesh distortion that occur during the simulation of SDF [10, 11]. Recently, Bao *et al.* [2] introduced an energy-stable numerical scheme based on a novel surface energy matrix for solving the motion of closed curves under anisotropic surface diffusion. This approach has been further developed and extended in several works, including [4, 5, 36–39, 54]. Duan and Li [20] proposed a novel class of PFEM to solve the surface evolution problem of geometric flow by using a new type of artificial tangential velocity. This approach effectively maintains good mesh quality, particularly when the time step is sufficiently small.

However, most existing methods for geometric flows are generally restricted to first-order accuracy in time discretization. Recently, Jiang *et al.* [27] proposed stable BGN/BDFk schemes for several isotropic flows, including mean curvature flow, SDF, and Willmore flow. Nevertheless, the development of high-order temporal schemes for anisotropic geometric evolution equations remains limited. Motivated by the approach [2] and the idea of stable

BGN/BDFk methods [27], we propose high-order BDFk schemes for anisotropic SDF. The high-order time schemes for anisotropic SDF considered here, are developed within the BGN framework and retain several advantages of the original BGN schemes, such as:

(i) High efficiency. They only require solving a system of linear algebraic equations at each time step, enabling fast execution.

(ii) Consistent maintenance of good mesh quality throughout the evolution of geometric flows, ensuring accurate numerical results.

SSD with surface diffusion as its primary kinetic feature, is a phenomenon observed in physics and materials science within solid-solid-vapor systems. It describes the agglomeration of solid films on a substrate [45]. Under the influence of surface tension or capillary forces, a solid film adhered to a substrate is inherently unstable or metastable in its deposited state, often displaying complex morphological features during its evolution, such as edge retraction [17, 35, 48], faceting [31, 32, 50], pinch-off events [26, 34], and fingering instabilities [33, 51–53]. These phenomena are characteristic of SSD, cf. Fig. 2. The surface energy (density) of the film material is often highly dependent on its crystal orientation, a phenomenon known as surface energy anisotropy, which plays a significant role in influencing both the kinetics and morphological evolution. In recent years, various mathematical models and numerical methods have been developed for SSD problems — cf. e.g. Dziwnik *et al.* [21], Naffouti *et al.* [43], Huang *et al.* [24], Jiang *et al.* [26, 28–30], Dornel *et al.* [17], Wang *et al.* [46], Bao and Zhao [7], Li and Bao [40], Zhao *et al.* [55–57], Li *et al.* [36], Li and Zhou [39]. Similar to SDF, the numerical methods used in these works predominantly rely on first-order time discretization. In this paper, we aim to improve the time discretization of the anisotropic SSD problem by employing higher-order BGN/BDFk schemes.

The remainder of the paper is organized as follows. In Section 2, we review the variational formulation and BGN/BDF1 scheme for the anisotropic SDF, and then introduce high-order time discretization schemes for the anisotropic SDF using the BGN/BDFk schemes. Section 3 presents the extension of the BGN/BDFk schemes to simulate SSD of thin films under anisotropic surface diffusion. In Section 4, we perform extensive numerical experiments to validate the accuracy of the algorithms for the anisotropic SDF and SSD problems, and simulate the evolution of curves under different anisotropic surface energies. Finally, conclusions are drawn in Section 5.

2. BGN/BDFk Scheme for Anisotropic SDF

In this section, we review the variational formulation and the BGN/BDF1 scheme, followed by an introduction to the BGN/BDFk schemes for anisotropic SDF.

2.1. The variational formulation

By introducing a special matrix $\mathbf{Z}_k(\vec{n})$, the equivalent form of anisotropic surface diffusion described in (1.3) can be expressed as follows [2]:

$$\vec{n}\cdot\partial_t\vec{X} = \partial_{ss}\mu, \tag{2.1a}$$
$$\mu\vec{n} = -\partial_s\big(\mathbf{Z}_k(\vec{n})\partial_s\vec{X}\big), \tag{2.1b}$$

where $\mathbf{Z}_k(\vec{n})$ is a symmetric surface energy matrix, defined as

$$\mathbf{Z}_k(\vec{n}) = \gamma(\vec{n})I_2 - \vec{n}\vec{\xi}(\vec{n})^T - \vec{\xi}(\vec{n})\vec{n}^T + k(\vec{n})\vec{n}\vec{n}^T, \quad \forall\vec{n}\in\mathbb{S}^1$$

with $k(\vec{n}) : \mathbb{S}^1 \to \mathbb{R}^+$ denoting a stabilizing function. $\mathbf{Z}_k(\vec{n})$ and ξ have the following relationship:

$$\mathbf{Z}_k(\vec{n})\partial_s\vec{X} = \gamma(\vec{n})\vec{\tau} - (\vec{\xi}\cdot\vec{\tau})\vec{n} = \vec{\xi}^{\perp}.$$

We introduce a time-independent variable $\rho\in\mathbb{I}=[0,1]$ and parameterize $\Gamma(t)$ as

$$\Gamma(t) := \vec{X}(\rho,t) = \big(x(\rho,t), y(\rho,t)\big)^T : \mathbb{I}\times\mathbb{R}^+ \to \mathbb{R}^2.$$

The arc-length parameter s computed by

$$s(\rho,t) = \int_0^\rho \big|\partial_r\vec{X}(\rho,t)\big|\,\mathrm{d}r$$

satisfies the relations $\partial_\rho s = |\partial_\rho\vec{X}|$, $\mathrm{d}s = \partial_\rho s\mathrm{d}\rho = |\partial_\rho\vec{X}|\mathrm{d}\rho$. If there is no ambiguity, we do not distinguish between $\vec{X}(\rho,t)$ and $\vec{X}(s,t)$.

Define the functional space for the evolution of the closed curve $\Gamma(t)$ as

$$L^2(\mathbb{I}) := \left\{ u:\mathbb{I}\to\mathbb{R} \;\middle|\; \int_{\Gamma(t)}|u(s)|^2\mathrm{d}s = \int_{\mathbb{I}}|u(s(\rho,t))|^2\partial_\rho s\,\mathrm{d}\rho < +\infty \right\},$$

equipped with the L^2-inner product

$$(u,v)_{\Gamma(t)} := \int_{\Gamma(t)} u(s)v(s)\,\mathrm{d}s = \int_{\mathbb{I}} u\big(s(\rho,t)\big)v\big(s(\rho,t)\big)\partial_\rho s(\rho,t)\,\mathrm{d}\rho \quad \text{for all} \quad u,v\in L^2(\mathbb{I}),$$

which can be extended to $[L^2(\mathbb{I})]^2$ directly. Moreover, the Sobolev spaces are defined as

$$\begin{aligned}
&\mathbb{K} := H^1(\mathbb{I}) = \big\{u:\mathbb{I}\to\mathbb{R}:\ u\in L^2(\mathbb{I}), \partial_\rho u\in L^2(\mathbb{I})\big\},\\
&\mathbb{K}_p := H^1_p(\mathbb{I}) = \big\{u\in\mathbb{K}:\ u(0)=u(1)\big\},\\
&\mathbb{X}_p := \mathbb{K}_p\times\mathbb{K}_p.
\end{aligned}$$

Multiplying (2.1a) by test function $\varphi\in\mathbb{K}_p$, integrating the result over $\Gamma(t)$, and applying integration by parts gives

$$\big(\vec{n}\cdot\partial_t\vec{X},\varphi\big)_{\Gamma(t)} = (\partial_{ss}\mu,\varphi)_{\Gamma(t)} = -(\partial_s\mu,\partial_s\varphi)_{\Gamma(t)}. \tag{2.2}$$

Similarly, multiplying a test function $\vec{\omega} = (\omega_1,\omega_2)^T\in\mathbb{X}_p$ to (2.1b), we have

$$(\mu\vec{n},\vec{\omega})_{\Gamma(t)} = \big(-\partial_s\big[\mathbf{Z}_k(\vec{n})\partial_s\vec{X}\big],\vec{\omega}\big)_{\Gamma(t)} = \big(\mathbf{Z}_k(\vec{n})\partial_s\vec{X},\partial_s\vec{\omega}\big)_{\Gamma(t)}. \tag{2.3}$$

Combining (2.2) and (2.3) leads to the symmetric variational formulation for the anisotropic surface diffusion (2.1): Given an initial curve $\Gamma(0) := \vec{X}(\mathbb{I},0)$ with $\vec{X}(\rho,0) \in \mathbb{X}_p$, find the solution $\Gamma(t) := \vec{X}(\mathbb{I},t)$ with $\vec{X}(\cdot,t) \in \mathbb{X}_p$ and the chemical potential $\mu(\cdot,t) \in \mathbb{K}$ such that

$$\begin{aligned} &\left(\vec{n}\cdot\partial_t\vec{X},\varphi\right)_{\Gamma(t)} + (\partial_s\mu,\partial_s\varphi)_{\Gamma(t)} = 0 \qquad \text{for all} \quad \varphi \in \mathbb{K}_p, \\ &(\mu,\vec{n}\cdot\vec{\omega})_{\Gamma(t)} - \left(\mathbf{Z}_k(\vec{n})\partial_s\vec{X},\partial_s\vec{\omega}\right)_{\Gamma(t)} = 0 \qquad \text{for all} \quad \vec{\omega} \in \mathbb{X}_p. \end{aligned} \tag{2.4}$$

Remark 2.1. For $\gamma(\vec{n}) = \gamma(-\vec{n})$, we can choose an appropriate minimizing stabilizing function $k(\vec{n})$ to ensure the symmetric positive property of the matrix $\mathbf{Z}_k(\vec{n})$. According to [2], we have

(i) For $\gamma(\vec{n}) = 1+\beta\cos 2\theta$, $k(\vec{n}) = 4-2\gamma(\vec{n})+4\beta^2\gamma(\vec{n})^{-1}$.

(ii) For $\gamma(\vec{n}) = 1+\beta\cos 4\theta$, $k(\vec{n}) = 2\gamma(\vec{n})+(16\beta+16\beta^2)\gamma(\vec{n})^{-1}$.

(iii) For $\gamma(\vec{n}) = \left(|n_1|^4+|n_2|^4\right)^{1/4}$, $k(\vec{n}) = 2\gamma(\vec{n})^{-3}$.

(iv) For $\gamma(\vec{n}) = \left(|n_1|^6+|n_2|^6\right)^{1/6}$, $k(\vec{n}) = 2\gamma(\vec{n})^{-5}\left(n_1^4+n_1^2n_2^2+n_2^4\right)$.

2.2. BGN/BDF1 scheme

Let $\mathbb{I} = [0,1] = \bigcup_{j=1}^N I_j$ with the subintervals $I_j = [\rho_{j-1},\rho_j]$, $h = 1/N$ be the mesh size and the grid nodes $\rho_j = jh$ for $j = 0,1,\ldots,N$. Define the finite element subspace of $H^1(\mathbb{I})$ as

$$\begin{aligned} &\mathbb{K}^h := \mathbb{K}^h(\mathbb{I}) := \left\{u^h \in \mathscr{C}(\mathbb{I}) \cap \mathbb{K}(\mathbb{I}) :\ u^h\big|_{I_j} \in \mathbb{P}_1 \quad \text{for all} \quad j = 1,2,\ldots,N\right\} \subset \mathbb{K}, \\ &\mathbb{K}_p^h := \left\{u^h \in \mathbb{K}^h :\ u^h(0) = u^h(1)\right\} \subset \mathbb{K}_p, \\ &\mathbb{X}_p^h := \mathbb{K}_p^h \times \mathbb{K}_p^h \subset \mathbb{X}_p, \end{aligned}$$

where $\mathbb{P}_1$ is the set of all polynomials of degree at most one.

Define the mass-lumped inner product $(\cdot,\cdot)_{\Gamma_h}^h$ over Γ^h by

$$(u,v)_{\Gamma_h}^h := \frac{1}{2}\sum_{j=1}^N \left|\vec{X}_h(\rho_j) - \vec{X}_h(\rho_{j-1})\right| \left[(u\cdot v)(\rho_j^-) + (u\cdot v)(\rho_{j-1}^+)\right],$$

where $\vec{X}^h$ is a parameterization of Γ^h, $\vec{X}^h(\rho_j)$ are the vertices of the polygon Γ^h, and u, v scalar or vector piecewise continuous functions with possible jumps at the nodes $\{\rho_j\}_{j=1}^N$, and $u(\rho_j^\pm) = \lim_{\rho\to\rho_j^\pm} u(\rho)$. The polygon $\Gamma^h(t)$ is composed by ordered vectors $\{\vec{h}_j(t)\}_{j=1}^N$,

$$h_{\min}(t) := \min_{1\le j\le N} \left|\vec{h}_j(t)\right| > 0 \quad \text{with} \quad \vec{h}_j = \vec{X}_h(\rho_j) - \vec{X}_h(\rho_{j-1}), \quad j = 1,2,\ldots,N.$$

We denote

$$\vec{n}^h\big|_{I_j} = -\frac{(\vec{h}_j)^\perp}{|\vec{h}_j|} =: \vec{n}_j^h, \quad \vec{\tau}^h\big|_{I_j} = \frac{\vec{h}_j}{|\vec{h}_j|} =: \vec{\tau}_j^h, \quad \vec{\xi}^h\big|_{I_j} = \vec{\xi}(\vec{n}_j^h) =: \vec{\xi}_j^h,$$

where $|\vec{h}_j|$ is the length of the vector $\vec{h}_j$.

Let $\Gamma^h(0) := \vec{X}^h(\rho,0) \in \mathbb{X}_p^h$ be an interpolation of the initial curve $\vec{X}_0(s)$ in (1.4) satisfying $\vec{X}_0(0) = \vec{X}_0(L_0)$, which is defined as $\vec{X}^h(\rho_j,0) = \vec{X}_0(s_j^0)$ with $s_j^0 = L_0\rho_j$ for $j = 0,1,\ldots,N$. Now we can write the semi-discrete scheme of the variational formulation (2.4) as: Given an initial curve $\Gamma^h(0) := \vec{X}^h(\mathbb{I},0) \in \mathbb{X}_p^h$, find the solution $\Gamma^h(t) := \vec{X}^h(\mathbb{I},t) \in \mathbb{X}_p^h$ and $\mu^h(\cdot,t) \in \mathbb{K}_p^h$ such that

$$\begin{aligned}
&\left(\vec{n}^h \cdot \partial_t \vec{X}^h, \varphi^h\right)_{\Gamma_h}^h + \left(\partial_s \mu^h, \partial_s \varphi^h\right) = 0 \qquad \text{for all} \quad \varphi^h \in \mathbb{K}_p^h,\\
&\left(\mu^h, \vec{n}^h \cdot \vec{\omega}^h\right)_{\Gamma_h}^h - \left(\mathbf{Z}_k(\vec{n}^h)\partial_s \vec{X}^h, \partial_s \vec{\omega}^h\right)_{\Gamma_h}^h = 0 \quad \text{for all} \quad \vec{\omega}^h \in \mathbb{X}_p^h.
\end{aligned}$$

For a full discretization, we fix $\tau > 0$ as a uniform time step and take $t_m = m\tau$, $m = 0,1,2,\ldots$ as the discrete time levels. Let $\vec{X}^m \in \mathbb{X}^h$ and Γ^m be the approximations of $\vec{X}(\cdot,t_m)$ and $\Gamma(t_m)$, respectively. We set

$$\vec{h}_j^m := \vec{X}^m(\rho_j) - \vec{X}^m(\rho_{j-1}), \quad j = 1,2,\ldots,N.$$

The unit tangential vector $\vec{\tau}^m$ and the outward unit normal vector $\vec{n}^m$ can be computed as

$$\vec{\tau}^m = \frac{\vec{h}_j^m}{|\vec{h}_j^m|}, \qquad \vec{n}^m = -\frac{(\vec{h}_j^m)^\perp}{|\vec{h}_j^m|}.$$

The first-order BGN scheme (BGN/BDF1) is based on the backward Euler method in time and is stated as follows:

Let $\Gamma^0 = \vec{X}^0 \in \mathbb{X}_p^h$ be an initial curve. For $m \geq 0$, find a curve $\Gamma^{m+1} := \vec{X}^{m+1} \in \mathbb{X}_p^h$ and the chemical potential $\mu^{m+1} \in \mathbb{K}_p^h$ such that

$$\begin{aligned}
&\left(\frac{\vec{X}^{m+1} - \vec{X}^m}{\tau} \cdot \vec{n}^m, \varphi^h\right)_{\Gamma^m}^h + \left(\partial_s \mu^{m+1}, \partial_s \varphi^h\right)_{\Gamma^m}^h = 0 \quad \text{for all} \quad \varphi^h \in \mathbb{K}_p^h,\\
&\left(\mu^{m+1}, \vec{n}^m \cdot \vec{\omega}^h\right)_{\Gamma^m}^h - \left(\mathbf{Z}_k(\vec{n}^m)\partial_s \vec{X}^{m+1}, \partial_s \vec{\omega}^h\right)_{\Gamma^m}^h = 0 \quad \text{for all} \quad \vec{\omega}^h \in \mathbb{X}_p^h.
\end{aligned} \tag{2.5}$$

Remark 2.2. Bao *et al.* [2] introduced a symmetric variational formulation (2.4) by incorporating a surface energy matrix and constructed an energy-stable PFEM for the anisotropic SDF. On the other hand, $\vec{n}^m$ in (2.5) has been replaced by the time-weighted interface normals

$$\vec{n}^{m+1/2} = -\frac{1}{2}\left(\partial_s \vec{X}^m + \partial_s \vec{X}^{m+1}\right)^\perp$$

to ensure area-conservation [6]. This approach was further extended to three-dimensional surfaces in [4], while retaining the key properties observed in two dimensions.

2.3. High-order BGN/BDFk algorithms

In this section, we establish high-order temporal schemes based on BDFk methods. Using the Taylor expansion for approximation of the velocity $\partial_t \vec{X}$ gives

$$\partial_t\vec{X}(\cdot,t_{m+1})=\frac{1}{\tau}\left(\frac{3}{2}\vec{X}(\cdot,t_{m+1})-2\vec{X}(\cdot,t_m)+\frac{1}{2}\vec{X}(\cdot,t_{m-1})\right)+\mathscr{O}(\tau^2),$$
$$\partial_t\vec{X}(\cdot,t_{m+1})=\frac{1}{\tau}\left(\frac{11}{6}\vec{X}(\cdot,t_{m+1})-3\vec{X}(\cdot,t_m)+\frac{3}{2}\vec{X}(\cdot,t_{m-1})-\frac{1}{3}\vec{X}(\cdot,t_{m-2})\right)+\mathscr{O}(\tau^3),$$
$$\partial_t\vec{X}(\cdot,t_{m+1})=\frac{1}{\tau}\left(\frac{25}{12}\vec{X}(\cdot,t_{m+1})-4\vec{X}(\cdot,t_m)+3\vec{X}(\cdot,t_{m-1})-\frac{4}{3}\vec{X}(\cdot,t_{m-2})\right.$$
$$\left.+\frac{1}{4}\vec{X}(\cdot,t_{m-3})\right)\tau+\mathscr{O}(\tau^4).$$

Hence, the velocity is approximated with an error of $\mathscr{O}(\tau^k)$, $2\le k\le 4$ at the time level t_{m+1}. Utilizing the mass-lumped inner product with a suitable predictor $\tilde{\Gamma}^{m+1}$ approximating $\Gamma(t_{m+1})$, we arrive at the following high-order schemes, referred to as BGN/BDFk: For $k=2,3,4$ and $m\ge k-1$, find a curve $\Gamma^{m+1}:=\vec{X}^{m+1}\in\mathbb{X}_p^h$ and a chemical potential $\mu^{m+1}\in\mathbb{K}_p^h$ such that

$$\begin{aligned}&\left(\frac{p\vec{X}^{m+1}-\hat{\vec{X}}^m}{\tau}\cdot\tilde{\vec{n}}^{m+1},\varphi^h\right)^h_{\tilde{\Gamma}^{m+1}}+\left(\partial_s\mu^{m+1},\partial_s\varphi^h\right)^h_{\tilde{\Gamma}^{m+1}}=0 \qquad \text{for all}\quad \varphi^h\in\mathbb{K}_p^h,\\ &\left(\mu^{m+1},\tilde{\vec{n}}^{m+1}\cdot\vec{\omega}^h\right)^h_{\tilde{\Gamma}^{m+1}}-\left(\mathbf{Z}_k(\tilde{\vec{n}}^{m+1})\partial_s\vec{X}^{m+1},\partial_s\vec{\omega}^h\right)^h_{\tilde{\Gamma}^{m+1}}=0 \qquad \text{for all}\quad \vec{\omega}^h\in\mathbb{X}_p^h,\end{aligned}\tag{2.6}$$

where

$$\mathbf{Z}_k(\tilde{\vec{n}}^{m+1})=\gamma(\tilde{\vec{n}}^{m+1})I_2-\tilde{\vec{n}}^{m+1}(\tilde{\vec{\xi}}^{m+1})^T-\tilde{\vec{\xi}}^{m+1}(\tilde{\vec{n}}^{m+1})^T+k(\tilde{\vec{n}}^{m+1})\tilde{\vec{n}}^{m+1}(\tilde{\vec{n}}^{m+1})^T,$$

$p,\hat{\vec{X}}^m$ are defined by

$$\textbf{BDF2}:\quad p=\frac{3}{2},\quad \hat{\vec{X}}^m=2\vec{X}^m-\frac{1}{2}\vec{X}^{m-1},\tag{2.7a}$$
$$\textbf{BDF3}:\quad p=\frac{11}{6},\quad \hat{\vec{X}}^m=3\vec{X}^m-\frac{3}{2}\vec{X}^{m-1}+\frac{1}{3}\vec{X}^{m-2},\tag{2.7b}$$
$$\textbf{BDF4}:\quad p=\frac{25}{12},\quad \hat{\vec{X}}^m=4\vec{X}^m-3\vec{X}^{m-1}+\frac{4}{3}\vec{X}^{m-2}-\frac{1}{4}\vec{X}^{m-3}.\tag{2.7c}$$

Besides,

$$\tilde{\vec{n}}^{m+1}=-\left(\frac{\partial_\rho\tilde{\vec{X}}^{m+1}}{|\partial_\rho\tilde{\vec{X}}^{m+1}|}\right)^\perp$$

is the normal vector, $\tilde{\Gamma}^{m+1}$ an approximation of $\Gamma(t_{m+1})$, $\tilde{\vec{\xi}}^{m+1}=\nabla\gamma(\tilde{\vec{n}}^{m+1})$ the Cahn-Hoffman vector and ∂_s the partial derivative based on the arc-length of $\tilde{\Gamma}^{m+1}$.

Following the work in [9], we can show the existence and uniqueness of the linear scheme (2.6) under certain weak assumptions on $\tilde{\Gamma}^{m+1}$.

Theorem 2.1 (Well-Posedness). *Let $k=2,3,4$ and $m\ge k-1$. If the BGN/BDFk schemes* (2.6) *satisfy the conditions*

(i) At least two vectors in $\{\tilde{\vec{h}}_j^m\}_{j=1}^N$ *are not parallel — i.e. there exist* $1 \le j_1 < j_2 \le N-1$ *such that*

$$\tilde{\vec{h}}_{j_1}^m \cdot \left(\tilde{\vec{h}}_{j_2}^m\right)^\perp \neq 0.$$

(ii) No degenerate vertex on $\tilde{\Gamma}^{m+1}$*, i.e.*

$$h_{\min}^m := \min_{1\le j\le N} \left|\tilde{\vec{h}}_j^{m+1}\right| = \min_{1\le j\le N} \left|\tilde{\vec{X}}^m(\rho_{j+1}) - \tilde{\vec{X}}^m(\rho_j)\right| > 0,$$

then they are well-posed — i.e. any system (2.6) *has a unique solution* $(\vec{X}^{m+1}, \mu^{m+1}) \in \mathbb{X}_p^h \times \mathbb{K}_p^h$.

To determine $\tilde{\Gamma}^{m+1}$ or $\tilde{\vec{X}}^{m+1}$ (which is equivalent to $\tilde{\Gamma}^{m+1}$), we predict $\tilde{\Gamma}^{m+1}$ using the solution from a lower-order BGN/BDFk scheme. This prediction is crucial for the effectiveness of the high-order BGN/BDFk schemes. For instance, the BGN/BDF1 scheme — i.e. the classical BGN1 scheme can be used to predict $\tilde{\Gamma}^{m+1}$ in the BGN/BDF2 scheme.

To start the BGN/BDFk algorithms, it is necessary to prepare the initial data $\vec{X}^0, \cdots, \vec{X}^{k-1}$ which should be approximations of $\vec{X}(\cdot,0), \cdots, \vec{X}(\cdot,t_{k-1})$ with an error of $\mathcal{O}(\tau^k)$. This can be achieved by using the BGN/BDF1 scheme with a finer time step. Specifically, to get an approximation of $\vec{X}(\cdot,t_1)$ with an error of $\mathcal{O}(\tau^k)$, for $k = 2,3,4$, it suffices to implement the BGN/BDF1 scheme with a time step size of $\tilde{\tau} \sim \tau^{k-1}$ by $\tau/\tilde{\tau}$ steps.

Now we introduce specific algorithms for the BGN/BDFk algorithms. In these algorithms, we write Γ^{m+1} and $\tilde{\Gamma}^{m+1}$ for polygonal curves described by $\vec{X}^{m+1}$ and $\tilde{\vec{X}}^{m+1}$, respectively.

Algorithm 2.1 BGN/BDF2

Require: An initial curve $\Gamma(0)$ approximated by a polygon Γ^0 with N vertices. Terminate time T and time step τ satisfy that T/τ is a positive integer.

1: Calculate $\vec{X}^1$ by using the BGN/BDF1 scheme (2.5) with Γ^0 and τ. Set $m = 1$.
2: **while** $m < T/\tau$ **do**
3: Use the BGN/BDF1 scheme (2.5) to compute $\tilde{\vec{X}}^{m+1}$ with Γ^m and τ.
4: Use the BGN/BDF2 scheme (2.6) and (2.7a) to compute $\vec{X}^{m+1}$ with $\vec{X}^{m-1}$, $\vec{X}^m$, $\tilde{\Gamma}^{m+1}$ and τ.
5: $m = m+1$.
6: **end while**

Algorithm 2.2 BGN/BDF3

Require: An initial curve $\Gamma(0)$ approximated by a polygon Γ^0 with N vertices. Terminate time T, time step τ and a finer time step $\tilde{\tau} \sim \tau^2$.

1: Calculate $\vec{X}^1$ by using the BGN/BDF1 scheme (2.5) with Γ^0 and $\tilde{\tau}$ for $\tau/\tilde{\tau}$ steps.
2: Calculate $\vec{X}^2$ by using the BGN/BDF1 scheme (2.5) with $\vec{X}^1$ and $\tilde{\tau}$ for another $\tau/\tilde{\tau}$ steps. Set $m = 2$.

3: **while** $m < T/\tau$ **do**
4: Use BGN/BDF2 Algorithm 2.1 to compute $\vec{\tilde{X}}^{m+1}$ with $\vec{X}^{m-1}$, $\vec{X}^{m}$ and τ.
5: Use the BGN/BDF3 scheme (2.6) and (2.7b) to compute $\vec{X}^{m+1}$ with $\vec{X}^{m-2}$, $\vec{X}^{m-1}$, $\vec{X}^{m}$, $\tilde{\Gamma}^{m+1}$ and τ.
6: $m = m + 1$.
7: **end while**

Algorithm 2.3 BGN/BDF4

Require: An initial curve $\Gamma(0)$ approximated by a polygon Γ^0 with N vertices. Terminate time T, time step τ and a finer time step $\tilde{\tau} \sim \tau^3$.
1: Calculate $\vec{X}^1$ by using the BGN/BDF1 scheme (2.5) with Γ^0 and $\tilde{\tau}$ for the first $\tau/\tilde{\tau}$ steps.
2: Calculate $\vec{X}^2$ by using the BGN/BDF1 scheme (2.5) with $\vec{X}^1$ and $\tilde{\tau}$ for the second $\tau/\tilde{\tau}$ steps.
3: Calculate $\vec{X}^3$ by using the BGN/BDF1 scheme (2.5) with $\vec{X}^2$ and $\tilde{\tau}$ for the third $\tau/\tilde{\tau}$ steps. Set $m = 3$.
4: **while** $m < T/\tau$ **do**
5: Use BGN/BDF3 Algorithm 2.2 to compute $\vec{\tilde{X}}^{m+1}$ with $\vec{X}^{m-2}$ $\vec{X}^{m-1}$, $\vec{X}^{m}$ and τ.
6: Use the BGN/BDF4 scheme (2.6) and (2.7c) to compute $\vec{X}^{m+1}$ with $\vec{X}^{m-3}$, $\vec{X}^{m-2}$, $\vec{X}^{m-1}$, $\vec{X}^{m}$, $\tilde{\Gamma}^{m+1}$ and τ.
7: $m = m + 1$.
8: **end while**

Remark 2.3. In [27], the BGN/BDF3 and BGN/BDF4 algorithms are proposed for isotropic flows, with $\vec{X}^2$ and $\vec{X}^3$ computed by using BGN/BDF2 and BGN/BDF3 schemes, respectively. However, while testing the convergence rates of these methods for anisotropic flows, we noted that the order of convergence is lower than our excepted results. In this work, for the BGN/BDF3 algorithm, we continue to use the BGN/BDF1 algorithm to compute $\vec{X}^2$ with a time step size of $\tilde{\tau} \sim \tau^2$ by taking $\tau/\tilde{\tau}$ steps. Similarly, within the BGN/BDF4 algorithm, we still use the BGN/BDF1 algorithm to compute $\vec{X}^3$ with a time step size of $\tilde{\tau} \sim \tau^3$ by taking $\tau/\tilde{\tau}$ steps. Numerous numerical experiments show that this modified approach is highly effective for the anisotropic SDFs and the SSD problems.

3. BGN/BDFk Algorithms for Simulating Anisotropic SSD

In this section, we review the anisotropic SSD problem [3, 28, 46] and build the corresponding BGN/BDFk schemes.

3.1. SSD problem and the variational formulation

As shown in Fig. 2, a typical problem in SSD involves studying the evolution of an open curve $\Gamma := \Gamma(t)$ in two dimensions. This process is governed by anisotropic surface

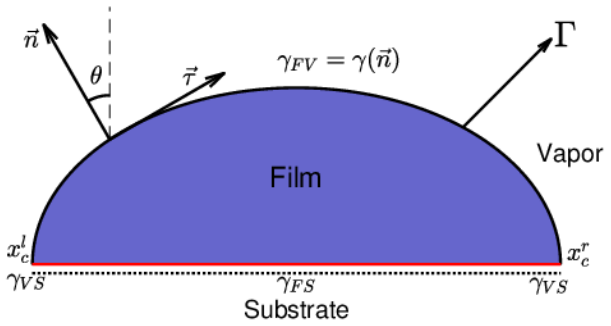

Figure 2: Schematic representation of solid films in two dimensions. γ_{FV}, γ_{VS}, and γ_{FS} represent the film vapor, vapor substrate and film substrate surface energy densities, respectively. x_c^l and x_c^r are the left and right contact points.

diffusion, where its two contact points $x_c^l := x_c^l(t)$ and $x_c^r := x_c^r(t)$ move along a rigid planar substrate. Note that all notations, except of the ones related to boundary conditions, remain the same as in the previous section.

We represent $\Gamma(t) = \vec{X}(s,t) = (x(s,t), y(s,t))^T$ with the arc-length parameter $s \in [0, L(t)]$ where $L(t)$ is the length of the curve. Alternatively, we can parameterize $\Gamma(t)$ as $\Gamma(t) = \vec{X}(\rho,t) = (x(\rho,t), y(\rho,t))^T$ with $\rho \in [0,1]$. For the SSD problem, according to [3, 28, 46], the open curve $\vec{X}(\rho,t)$ satisfies the anisotropic surface diffusion (1.3) and the following boundary conditions:

(i) The contact point condition

$$y(0,t) = 0, \quad y(1,t) = 0, \quad t \geq 0. \tag{3.1}$$

(ii) The relaxed contact angle condition

$$\frac{\mathrm{d}x_c^l}{\mathrm{d}t} = \eta\left(\xi_2|_{s=0} - \sigma\right), \quad \frac{\mathrm{d}x_c^r}{\mathrm{d}t} = -\eta\left(\xi_2|_{s=L} - \sigma\right), \quad t \geq 0. \tag{3.2}$$

(iii) The zero-mass flux condition

$$\partial_s \mu(0,t) = 0, \quad \partial_s \mu(1,t) = 0, \quad t \geq 0, \tag{3.3}$$

where $\sigma = (\gamma_{VS} - \gamma_{FS})/\gamma_{FV}$ with γ_{VS}, γ_{FS} and γ_{FV} representing the film/vapor, vapor/substrate and film/substrate surface energy densities, respectively. The parameter $\eta \in (0, \infty)$ indicates the contact line mobility and $\vec{\xi} = (\xi_1, \xi_2)^T$ is the dimensionless Cahn-Hoffman vector. In addition, we assume that $x_c^l(t)$ and $x_c^r(t)$ satisfy $x_c^l(t) = x(0,t) \leq x_c^r(t) = x(1,t)$.

Introduce the Sobolev spaces

$$\begin{aligned}
&H^1(\mathbb{I}) := \left\{u : \mathbb{I} \to \mathbb{R}, \text{ and } u \in L^2(\mathbb{I}), \partial_\rho u \in L^2(\mathbb{I})\right\},\\
&H_0^1(\mathbb{I}) := \left\{u : \mathbb{I} \to \mathbb{R}, \text{ and } u \in H^1(\mathbb{I}), u(0) = u(1) = 0\right\},\\
&\mathbb{X} := H^1(\mathbb{I}) \times H_0^1(\mathbb{I}).
\end{aligned}$$

Following [36], we multiply the test function $\phi \in H^1(\mathbb{I})$ by (2.1a), integrate the result over $\Gamma(t)$ by using integration by parts, and consider the zero mass flux condition (3.3), thus obtaining

$$\left(\vec{n}\cdot\partial_t\vec{X},\varphi\right)_{\Gamma(t)} = (\partial_{ss}\mu,\varphi)_{\Gamma(t)} = -(\partial_s\mu,\partial_s\varphi)_{\Gamma(t)}. \tag{3.4}$$

Similarly, multiplying the test function $\vec{\omega} = (\omega_1,\omega_2)^T \in (\mathbb{X})$ by (2.1b), integrating over $\Gamma(t)$, performing integration by parts, considering the relaxed contact angle condition (3.2), and using the relation (2.1) gives

$$\begin{aligned}(\mu\vec{n},\vec{\omega})_{\Gamma(t)} &= \left(-\partial_s\left[\mathbf{Z}_k(\vec{n})\partial_s\vec{X}\right],\vec{\omega}\right)_{\Gamma(t)}\\ &= \left(\mathbf{Z}_k(\vec{n})\partial_s\vec{X},\partial_s\vec{\omega}\right)_{\Gamma(t)} - \vec{\xi}^{\perp}\cdot\vec{\omega}\big|_{\rho=0}^{\rho=1}\\ &= \left(\mathbf{Z}_k(\vec{n})\partial_s\vec{X},\partial_s\vec{\omega}\right)_{\Gamma(t)} + \frac{1}{\eta}\left[\frac{\mathrm{d}x_c^l}{\mathrm{d}t}\omega_1(0) + \frac{\mathrm{d}x_c^r}{\mathrm{d}t}\omega_1(1)\right]\\ &\quad - \sigma[\omega_1(1)-\omega_1(0)].\end{aligned} \tag{3.5}$$

Combining (3.4) and (3.5) leads to the following symmetric variational formulation of the anisotropic SDF (2.5) with the boundary conditions (3.1)-(3.3): Given an initial open curve $\Gamma(0) = \vec{X}(\mathbb{I},0) \in \mathbb{X}$ with taking $x_c^l(t) = x(0,t) \le x_c^r(t) = x(1,t)$, find the solution $\Gamma(t) := \vec{X}(\mathbb{I},t) \in \mathbb{X}$, and the chemical potential $\mu(\cdot,t) \in H^1(\mathbb{I})$ such that

$$\begin{aligned}&\left(\vec{n}\cdot\partial_t\vec{X},\varphi\right)_{\Gamma(t)} + (\partial_s\mu,\partial_s\varphi)_{\Gamma(t)} = 0 \quad \text{for all} \quad \varphi\in H^1(\mathbb{I}),\\ &(\mu\vec{n},\vec{\omega})_{\Gamma(t)} - \left(\mathbf{Z}_k(\vec{n})\partial_s\vec{X},\partial_s\vec{\omega}\right)_{\Gamma(t)} - \frac{1}{\eta}\left[\frac{\mathrm{d}x_c^l}{\mathrm{d}t}\omega_1(0) + \frac{\mathrm{d}x_c^r}{\mathrm{d}t}\omega_1(1)\right]\\ &\quad + \sigma[\omega_1(1)-\omega_1(0)] = 0 \qquad \text{for all} \quad \vec{\omega}\in\mathbb{X}.\end{aligned}$$

3.2. BGN/BDFk algorithms

Define the finite element subspaces

$$\begin{aligned}&\mathbb{K}^h := \left\{u\in\mathscr{C}(\mathbb{I}) \;\middle|\; u\big|_{I_j}\in\mathbb{P}_1 \quad \text{for all} \quad j=1,2,\ldots,N\right\}\subseteq H^1(\mathbb{I}),\\ &\mathbb{K}_0^h := \mathbb{K}^h\cap H_0^1(\mathbb{I}),\\ &\mathbb{X}^h := \mathbb{K}^h\times\mathbb{K}_0^h.\end{aligned}$$

We first establish the following BGN/BDF1 scheme: Given an initial curve $\Gamma^0 = \vec{X}^0 \in \mathbb{X}^h$, find the solution $\Gamma^{m+1} := \vec{X}^{m+1} \in \mathbb{X}^h$ and the chemical potential $\mu^{m+1} \in \mathbb{K}^h$ such that

$$\begin{aligned}&\left(\frac{\vec{X}^{m+1}-\vec{X}^m}{\tau}\cdot\vec{n}^m,\varphi^h\right)_{\Gamma^m}^h + \left(\partial_s\mu^{m+1},\partial_s\varphi^h\right)_{\Gamma^m}^h = 0 \qquad \text{for all} \quad \varphi\in\mathbb{K}^h,\\ &\left(\mu^{m+1},\vec{n}^m\cdot\vec{\omega}^h\right)_{\Gamma^m}^h - \left(\mathbf{Z}_k(\vec{n}^m)\partial_s\vec{X}^{m+1},\partial_s\vec{\omega}^h\right)_{\Gamma^m}^h + \sigma\left[\omega_1^h(1)-\omega_1^h(0)\right]\\ &\quad - \frac{1}{\eta}\left[\frac{x_l^{m+1}-x_l^m}{\tau}\omega_1^h(0) + \frac{x_r^{m+1}-x_r^m}{\tau}\omega_1^h(1)\right] = 0 \quad \text{for all} \quad \vec{\omega}^h\in\mathbb{X}^h,\end{aligned}$$

where $x_l^{m+1} = x^{m+1}(0) \le x_r^{m+1} = x^{m+1}(1)$.

Similarly, we can also establish high-order temporal scheme based on the BDFk methods. By utilizing the mass-lumped inner product with a suitable predictor $\tilde{\Gamma}^{m+1}$, which approximates $\Gamma(t_{m+1})$, we derive the following high-order schemes, referred to as BGN/BDFk schemes: For $k=2,3,4$, $m\geq k-1$, find a solution $\Gamma^{m+1}=\vec{X}^{m+1}\in\mathbb{X}^h$ and a chemical potential $\mu^{m+1}\in\mathbb{K}^h$, $m\geq 0$ such that

$$\begin{aligned}
&\left(\frac{p\vec{X}^{m+1}-\hat{\vec{X}}^m}{\tau}\cdot\tilde{\vec{n}}^{m+1},\varphi^h\right)^h_{\tilde{\Gamma}^{m+1}}+\left(\partial_s\mu^{m+1},\partial_s\varphi^h\right)^h_{\tilde{\Gamma}^{m+1}}=0\quad\text{for all}\quad\varphi\in\mathbb{K}^h,\\
&\left(\mu^{m+1},\tilde{\vec{n}}^{m+1}\cdot\vec{\omega}^h\right)^h_{\tilde{\Gamma}^{m+1}}-\left(\mathbf{Z}_k(\tilde{\vec{n}}^{m+1})\partial_s\vec{X}^{m+1},\partial_s\vec{\omega}^h\right)^h_{\tilde{\Gamma}^{m+1}}+\sigma\left[\omega_1^h(1)-\omega_1^h(0)\right]\\
&\quad-\frac{1}{\eta}\left[\frac{px_l^{m+1}-\hat{x}_l^m}{\tau}\omega_1^h(0)+\frac{px_r^{m+1}-\hat{x}_r^m}{\tau}\omega_1^h(1)\right]=0\qquad\text{for all}\quad\vec{\omega}^h\in\mathbb{X}^h,
\end{aligned}\tag{3.6}$$

where

$$x_l^{m+1}=x^{m+1}(0)\leq x_r^{m+1}=x^{m+1}(1).$$

All notations remain the same as in Section 2.3, and the terms $p,\hat{\vec{X}}^m,\hat{x}_l^m,\hat{x}_r^m$ are defined by

$$\begin{aligned}
\text{BDF2:}\quad p&=\frac{3}{2},\quad \hat{X}^m=2\bar{X}^m-\frac{1}{2}\bar{X}^{m-1},\\
&\quad\ \hat{x}_l^m=2x_l^m-\frac{1}{2}x_l^{m-1},\quad \hat{x}_r^m=2x_r^m-\frac{1}{2}x_r^{m-1},\\
\text{BDF3:}\quad p&=\frac{11}{6},\quad \hat{X}^m=3\bar{X}^m-\frac{3}{2}\bar{X}^{m-1}+\frac{1}{3}\bar{X}^{m-2},\\
&\quad\ \hat{x}_l^m=3x_l^m-\frac{3}{2}x_l^{m-1}+\frac{1}{3}x_l^{m-2},\\
&\quad\ \hat{x}_r^m=3x_r^m-\frac{3}{2}x_r^{m-1}+\frac{1}{3}x_r^{m-2},\\
\text{BDF4:}\quad p&=\frac{25}{12},\quad \hat{X}^m=4\bar{X}^m-3\bar{X}^{m-1}+\frac{4}{3}\bar{X}^{m-2}-\frac{1}{4}\bar{X}^{m-3},\\
&\quad\ \hat{x}_l^m=4x_l^m-3x_l^{m-1}+\frac{4}{3}x_l^{m-2}-\frac{1}{4}x_l^{m-3},\\
&\quad\ \hat{x}_r^m=4x_r^m-3x_r^{m-1}+\frac{4}{3}x_r^{m-2}-\frac{1}{4}x_r^{m-3}.
\end{aligned}$$

We can also obtain the well-posedness of the BGN/BDFk schemes (3.6), which can be proved similar to [9].

Remark 3.1. For the BGN/BDF1 scheme, the numerical convergence rate $\mathcal{O}(h^2)$ can only be observed for $\tau=h^2$. Additionally, Duan and Li [20] stated that the BGN/BDF1 scheme is unstable for sufficiently small values of τ. One advantage of using high-order schemes is that very small time step τ is not required to achieve the desired convergence rate for numerical experiments.

4. Numerical Results

In this section, the results of numerical simulations of the SDF and SSD problems by proposed BGN/BDFk schemes are presented. We consider different types of surface energy anisotropy for various initial geometries. In particular, the following types of surface energy anisotropies are discussed [2].

Case I. The 2-fold anisotropic surface energy $\gamma(\vec{n}) = \gamma(\theta) = 1 + \beta\cos(2\theta)$, $\beta \geq 0$, with

$$\vec{\xi} = \vec{\xi}(\vec{n}) = \vec{n} + \beta\cos(2\theta)\vec{n} + 2\beta\sin(2\theta)\vec{n}^{\perp},$$
$$k(\vec{n}) = 4 - 2\gamma(\vec{n}) + \frac{4\beta^2}{\gamma(\vec{n})}.$$

Case II. The 4-fold anisotropic surface energy $\gamma(\vec{n}) = 1 + \beta\cos(4\theta)$, $\beta \geq 0$, with

$$\vec{\xi} = \vec{\xi}(\vec{n}) = \vec{n} + \beta\cos(4\theta)\vec{n} + 4\beta\sin(4\theta)\vec{n}^{\perp},$$
$$k(\vec{n}) = 2\gamma(\vec{n}) + \frac{16\beta + 16\beta^2}{\gamma(\vec{n})}.$$

Case III. The l^4-norm metric anisotropic surface energy $\gamma(\vec{n}) = \|\vec{n}\|_{l^4} = (|n_1|^4 + |n_2|^4)^{1/4}$, with

$$\vec{\xi} = \vec{\xi}(\vec{n}) = \gamma(\vec{n})^{-3}\begin{pmatrix} |n_1|^2 n_1 \\ |n_2|^2 n_2 \end{pmatrix},$$
$$k(\vec{n}) = 2\gamma(\vec{n})^{-3}.$$

Case IV. The l^6-norm metric anisotropic surface energy $\gamma(\vec{n}) = \|\vec{n}\|_{l^6} = (|n_1|^6 + |n_2|^6)^{1/6}$, with

$$\vec{\xi} = \vec{\xi}(\vec{n}) = \gamma(\vec{n})^{-5}\begin{pmatrix} |n_1|^4 n_1 \\ |n_2|^4 n_2 \end{pmatrix},$$
$$k(\vec{n}) = 2\gamma(\vec{n})^{-5}\left(n_2^4 + n_2^2 n_1^2 + n_1^4\right).$$

We test the convergence rates of the BGN/BDFk schemes for different curves. To calculate the difference between curves Γ_1 and Γ_2, we use the manifold distance $M(\Gamma_1, \Gamma_2)$ introduced in [57]. The manifold distance $M(\Gamma_1, \Gamma_2)$ is defined as

$$M(\Gamma_1, \Gamma_2) := |(\Omega_1 \setminus \Omega_2) \cup (\Omega_2 \setminus \Omega_1)| = |\Omega_1| + |\Omega_2| - 2|\Omega_1 \cap \Omega_2|,$$

where the area of Ω is represented as $|\Omega|$.

In order to obtain grid distributions in different situations, we define the grid ratio $\Phi(t)$ of the curve $\Gamma^h(t)$ by

$$\Phi(t) = \frac{h_{\max}^m}{h_{\min}^m} = \frac{\max_{1\leq j\leq N}|\vec{h}_j(t)|}{\min_{1\leq j\leq N}|\vec{h}_j(t)|}, \quad m \geq 0.$$

The total interface free energy $W^h(t)$ of a closed curve is defined as

$$W^h(t) = \int_{\Gamma(t)} \gamma(\vec{n}) \mathrm{d}s, \quad t \geq 0.$$

The total interface free energy $W^h(t)$ of SSD is defined as

$$W^h(t) = \int_{\Gamma(t)} \gamma(\vec{n}) \mathrm{d}s - \sigma\big(x_c^r(t) - x_c^l(t)\big), \quad t \geq 0.$$

4.1. Anisotropic SDF

For the anisotropic SDF, we mainly do the following tests:

1. Check the convergence order of BGN/BDFk schemes for the SDF for different type of the surface energy anisotropy. To this end, we set $\tau^k = h^2$ in convergence tests. Fig. 3 shows the comparison of temporal convergence rates of BGN/BDFk schemes at time $T = 1$. The numerical results indicate that the numerical error of the BGN/BDFk schemes converge at expected k-th order.

2. Next, we examine the mesh quality of the BGN/BDFk schemes for the SDF for different type of the surface energy anisotropys. Fig. 4 shows that during long-term simulations, the mesh distribution functions approach a constant. Additionally, the graphs show that higher-order algorithms approach a constant faster than lower-order ones, demonstrating that the higher-order BGN/BDFk schemes have an advantage in improving mesh quality.

3. We also test the normalized free energy $W^h(t)/W^h(0)$. Fig. 5 demonstrates that BGN/BDFk schemes for the SDF with different type of anisotropic energy functions exhibit energy stability.

4. Finally, we use BGN/BDFk schemes to study the morphological evolution for different anisotropic surface energies. The blue solid lines represent the initial curves, the black dashed lines show the curves during the evolution process, and the red solid lines indicate the final equilibrium shapes. Figs. 6-9 illustrate the evolution of initial elliptical curves toward their equilibrium shapes, Fig. 10 shows the evolution of an initial flower-shaped curve, and Fig. 11 presents the evolution of a rectangular curve with two sides formed by half-ellipses. The experiments show that the equilibrium states achieved by the higher-order schemes are consistent with the ones obtained by the BGN/BDF1 scheme.

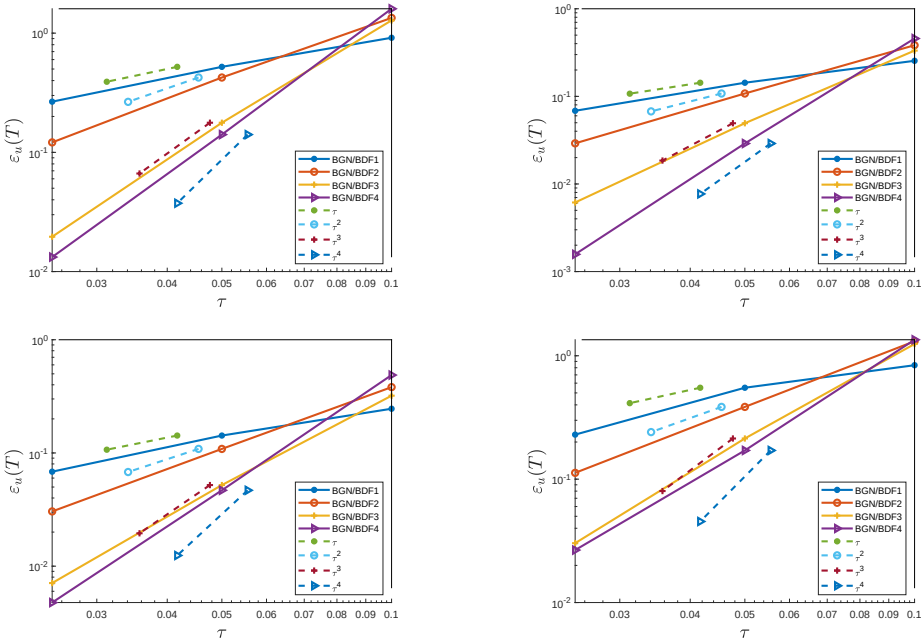

Figure 3: Time convergence rates $\epsilon_u(T)$ of the BGN/BDFk schemes (2.6) on closed curves. Top left: Case I, $\beta = 1/20$; Top right: Case II, $\beta = 1/20$; Bottom left: Case III; Bottom right: Case IV. Initial curve is an ellipse with major axis 4 and minor axis 2. The time step and spatial step are both 0.1.

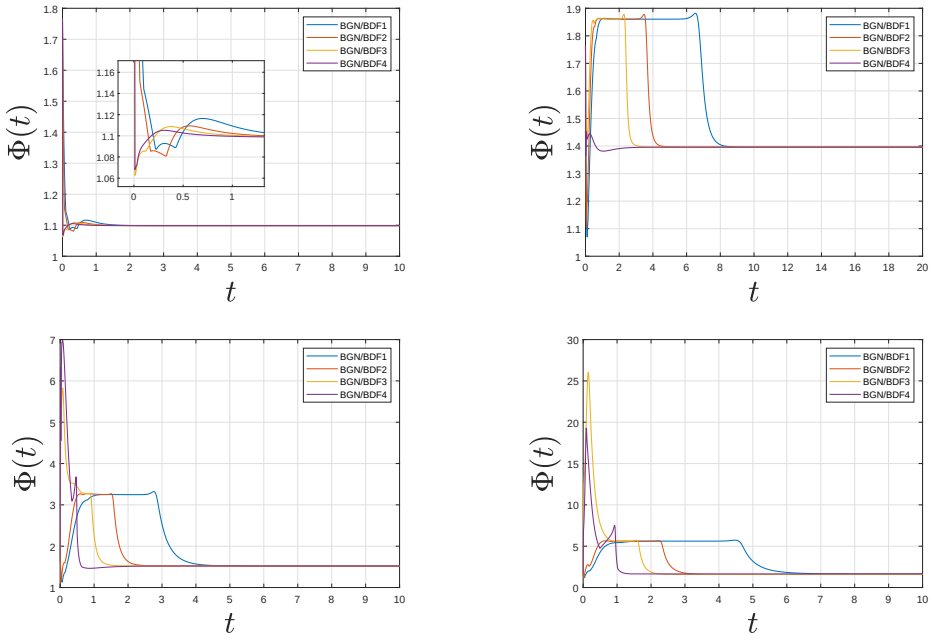

Figure 4: Mesh ratio $\Phi(t)$ for BGN/BDFk schemes (2.6) on closed curves. Top left: Case I, $\beta = 1/20$. Top right: Case II, $\beta = 1/20$. Bottom left: Case III. Bottom right: Case IV. Initial curve is an ellipse with major axis 4 and minor axis 2. The time step is 0.01, the spatial step is to 0.1.

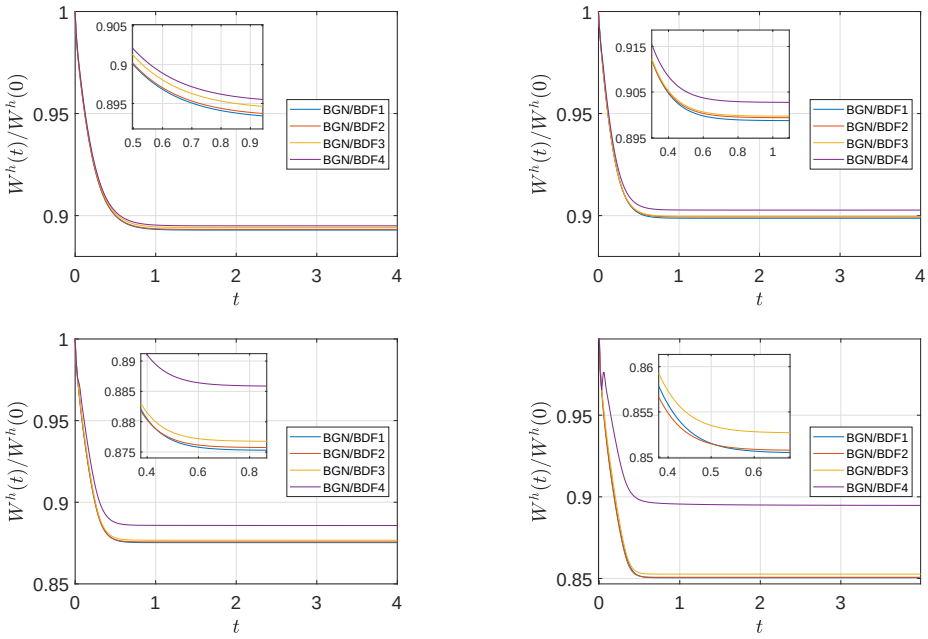

Figure 5: The normalized energy $w^h(t)/w^h(0)$ of the BGN/BDFk schemes (2.6) on closed curves. Top left: Case I, $\beta = 1/20$; Top right: Case II, $\beta = 1/20$; Bottom left: Case III; Bottom right: Case IV. Initial curve is an ellipse with major axis 4 and minor axis 2. The time step and spatial step are both 0.01.

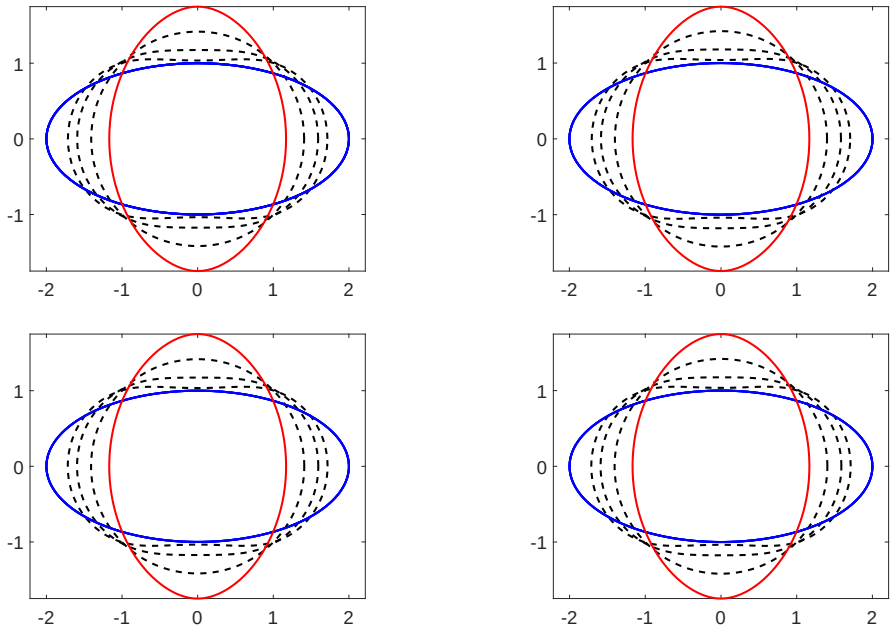

Figure 6: The evolution of closed curves with 2-fold anisotropy. Initial curve is an ellipse with major axis 4 and minor axis 2, and $\beta = 1/5$. Top left: $h = 10^{-2}, \tau = h^2$; Top right: $h = 10^{-2}, \tau^2 = h^2$; Bottom left: $h = 10^{-2}, \tau^3 = h^2$; Bottom right: $h = 1/1600, \tau^4 = h^2$.

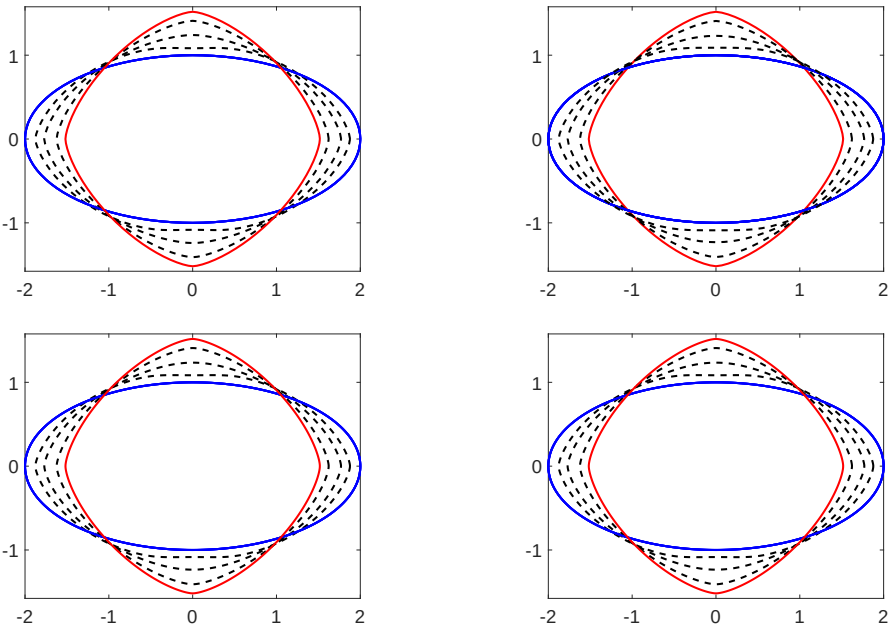

Figure 7: The evolution of closed curves with 4-fold anisotropy. Initial curve is an ellipse with major axis 4 and minor axis 2, and $\beta = 1/17$. Top left: $h = 10^{-2}, \tau = h^2$; Top right: $h = 10^{-2}, \tau^2 = h^2$; Bottom left: $h = 10^{-2}, \tau^3 = h^2$; Bottom right: $h = 1/1600, \tau^4 = h^2$.

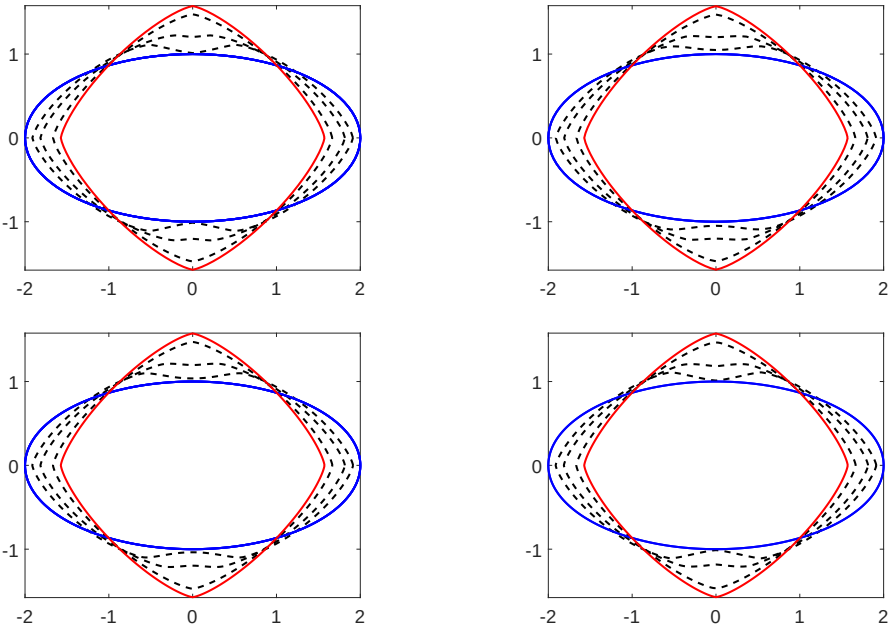

Figure 8: The evolution of closed curves with l^4-norm anisotropy. Initial curve is an ellipse with major axis 4 and minor axis 2. Top left: $h = 10^{-2}, \tau = h^2$; Top right: $h = 10^{-2}, \tau^2 = h^2$; Bottom left: $h = 10^{-2}, \tau^3 = h^2$; Bottom right: $h = 1/1600, \tau^4 = h^2$.

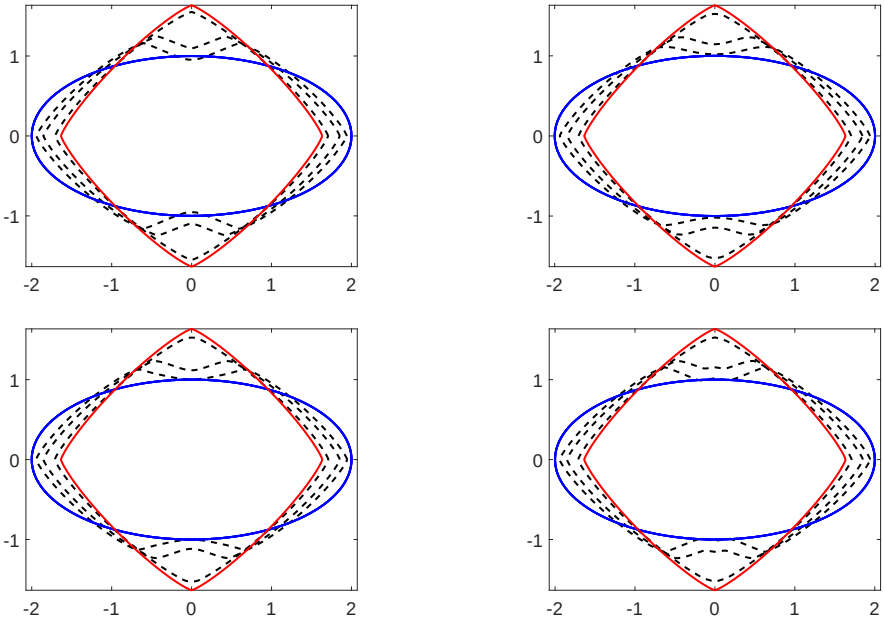

Figure 9: The evolution of closed curves with l^6-norm anisotropy. Initial curve is an ellipse with major axis 4 and minor axis 2. Top left: $h = 10^{-2}, \tau = h^2$; Top right: $h = 10^{-2}, \tau^2 = h^2$; Bottom left: $h = 10^{-2}, \tau^3 = h^2$; Bottom right: $h = 1/1600, \tau^4 = h^2$.

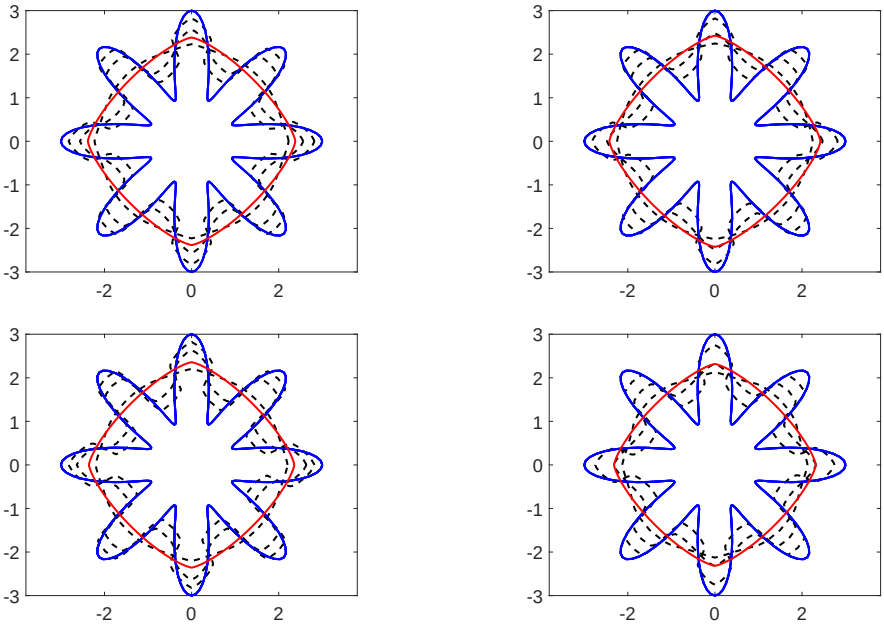

Figure 10: The evolution of closed curves with l^4-norm anisotropy. Initial curve is a flower and its parametric equation is $x = (2 + \cos(16\pi\rho))\cos(2\pi\rho), y = (2 + \cos(16\pi\rho))\sin(2\pi\rho)$. Top left: $h = 1/200, \tau = 10^{-3}$; Top right: $h = 1/200, \tau = 10^{-3}$; Bottom left: $h = 1/200, \tau = 10^{-3}$; Bottom right $h = 1/200, \tau = 4 \times 10^{-3}$.

4.2. Anisotropic SSD

For the anisotropic SSD problem, we set $\eta = 100$ and $\sigma = -0.6$ and do the following tests:

1. We plot the errors of BGN/BDFk schemes for the SSD problems for various anisotropic surface energy at fixed time $T = 1$. For $\tau^k = h^2$, Fig. 12 shows that the BGN/BDFk schemes achieve the convergence rate $\mathcal{O}(h^2 + \tau^k)$, consistent with our expectations.

2. We next evaluate the mesh quality throughout the evolution of the BGN/BDFk schemes for the SSD problems, considering four distinct types of anisotropic surface energy functions. Fig. 13 demonstrates that the mesh function $\psi(t)$ eventually converges to a constant over time. Similar to the SDF case, we observe that in higher-order schemes, $\psi(t)$ approaches this constant more rapidly than in lower-order schemes.

3. Additionally, we analyze the time evolution of the total free energy computed by the BGN/BDFk schemes. As Fig. 14 shows, for various anisotropic surface energies and BGN/BDFk schemes, the normalized total free energy $W^h(t)/W^h(0)$ consistently decreases over the course of the evolution.

4. Finally, we present several numerical tests to demonstrate the morphological evolution of different island films toward their respective equilibrium shapes during SSD, under various anisotropic surface energies and different BGN/BDFk schemes. Using Figs. 15-20, we can conclude that, regardless of the initial curves, they consistently evolve toward the equilibrium state associated with the anisotropic surface energy.

5. Conclusions

In this paper, we develop novel higher-order temporal PFEMs for solving anisotropic SDF and anisotropic SSD problem. These methods are based on the classical BGN formulation utilizing BDFk schemes for time discretization and combining with linear finite element approximations in space. Numerical experiments have demonstrated that the BGN/BDFk schemes achieve second-order spatial accuracy and k-th order temporal accuracy. Although we have not yet provided a theoretical proof of the energy dissipation property for the BGN/BDFk schemes, the numerical results consistently indicate that they ensure energy dissipation throughout the evolution. Additionally, the proposed schemes maintain good mesh quality during the entire simulation process. We also investigate the long-term behavior of the schemes toward equilibrium for different anisotropic surface energies, further validating their robustness and reliability.

Acknowledgments

This research was supported by the National Natural Science Foundation of China (Grant Nos. 11801527, U23A2065).

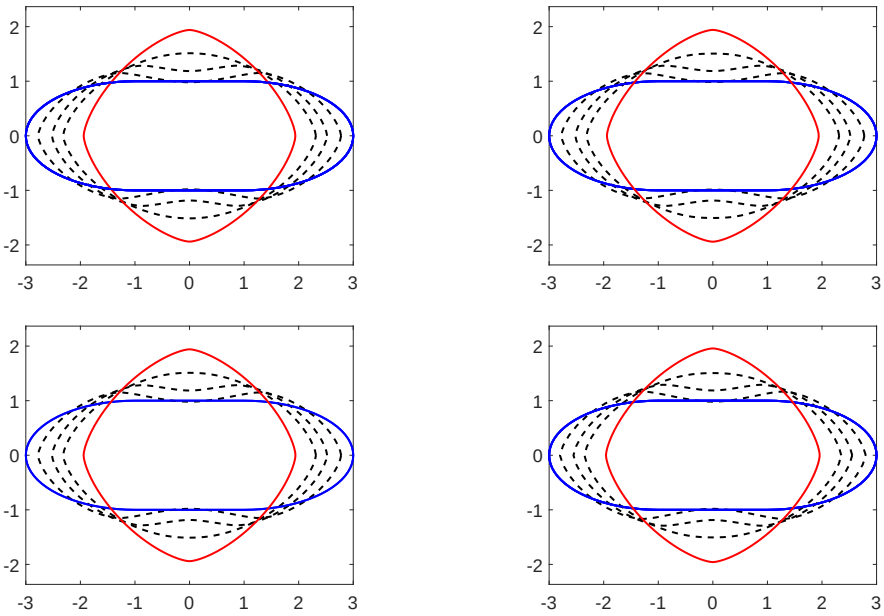

Figure 11: The evolution of closed curves with 4-fold anisotropy. Initial curve is an ellipse with major axis 4 and minor axis 2, divided into two halves, connected by two segments of length 2 in the middle, and $\beta = 1/17$. Top left: $h = 1/120, \tau = 10^{-2}$; Top right: $h = 1/120, \tau = 10^{-2}$; Bottom left: $h = 1/120, \tau = 10^{-2}$; Bottom right: $h = 1/120, \tau = 10^{-2}$.

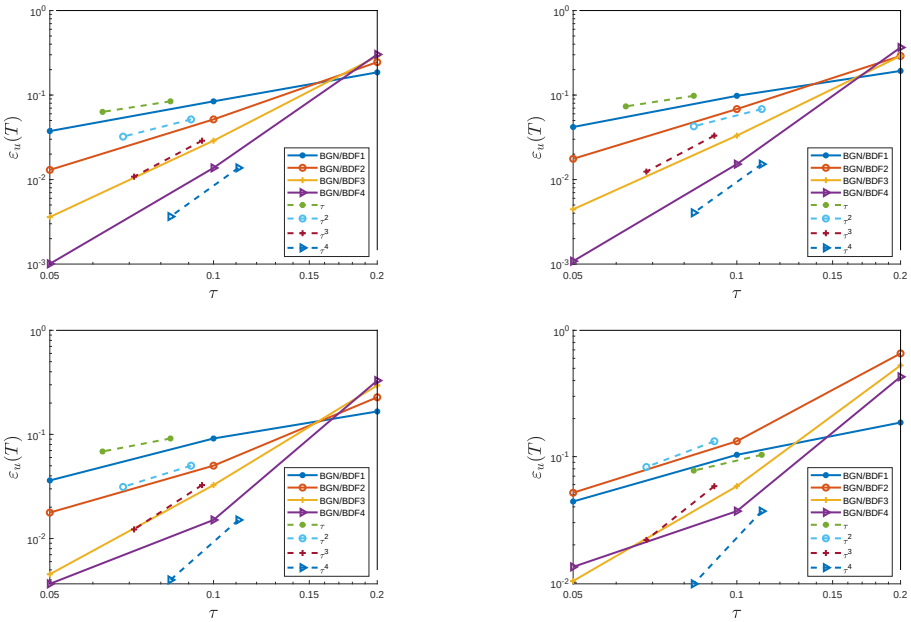

Figure 12: Time convergence rates $\epsilon_u(T)$ for the BGN/BDFk schemes (3.6) on SSD. Top left: Case I, $\beta = 1/20$ and $\sigma = -0.6$; Top right: Case II, $\beta = 1/20$ and $\sigma = -0.2$; Bottom left: Case III, $\sigma = -0.6$; Bottom right: Case IV, $\sigma = -0.2$. Initial curve is the upper half of an ellipse with major axis 4 and minor axis 2. The time step and spatial step are both 0.2.

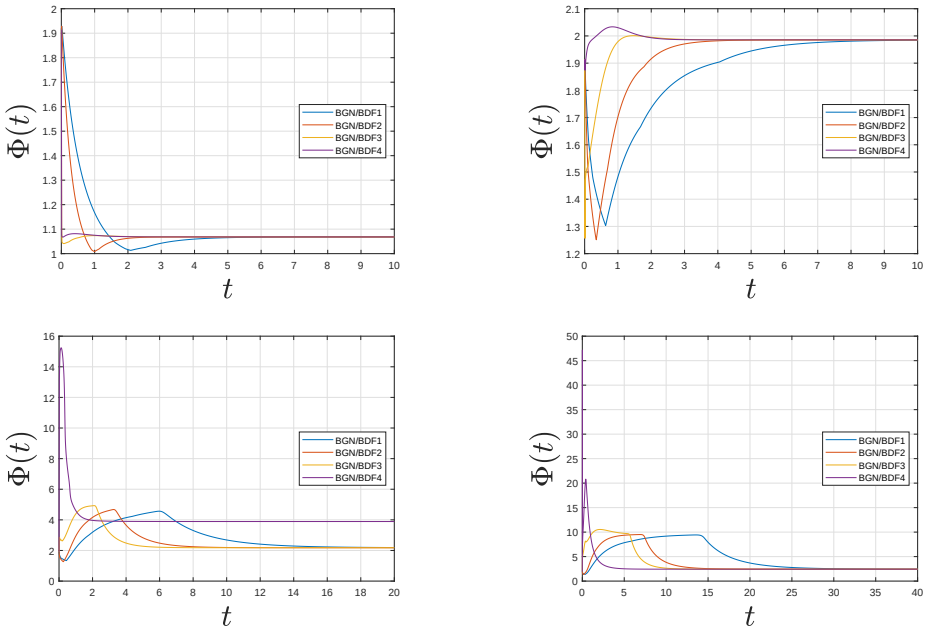

Figure 13: Mesh ratio $\Phi(t)$ for the BGN/BDFk schemes (3.6) on SSD. Top left: Case I, $\beta = 1/20$; Top right: Case II, $\beta = 1/20$; Bottom left: Case III; Bottom right: Case IV. Initial curve is the upper half of an ellipse with major axis 4 and minor axis 2. The time step and spatial step are both 0.2.

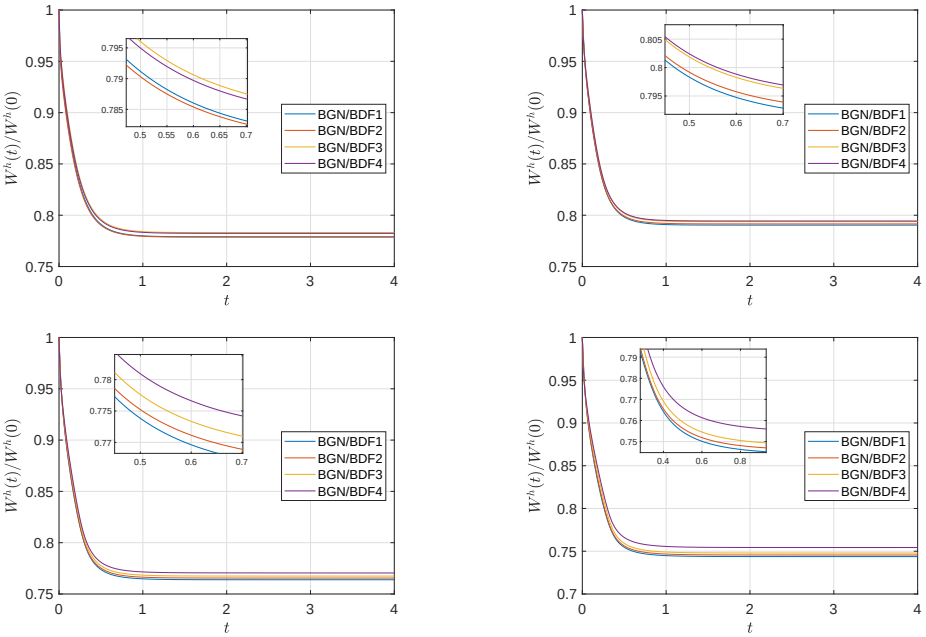

Figure 14: The normalized energy $w^h(t)/w^h(0)$ of the BGN/BDFk schemes (3.6) on SSD. Top left: Case I, $\beta = 1/20$. Top right: Case II, $\beta = 1/20$. Bottom left: Case III. Bottom right: Case IV. Initial curve is the upper half of an ellipse with major axis 4 and minor axis 2. The time step and spatial step are both 0.01.

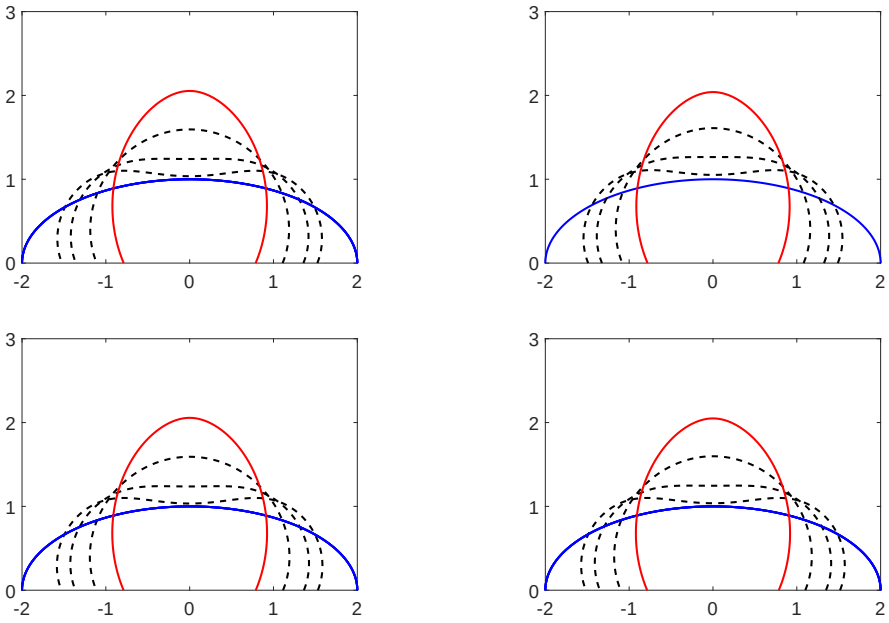

Figure 15: The evolution of SSD with 2-fold anisotropy. Initial curve is the upper half of an ellipse with major axis 4 and minor axis 2. $\beta = 1/5$. Top left: $h = 10^{-2}, \tau = h^2$; Top right: $h = 10^{-2}, \tau^2 = h^2$; Bottom left: $h = 10^{-2}, \tau^3 = h^2$; Bottom right: $h = 1/1600, \tau^4 = h^2$.

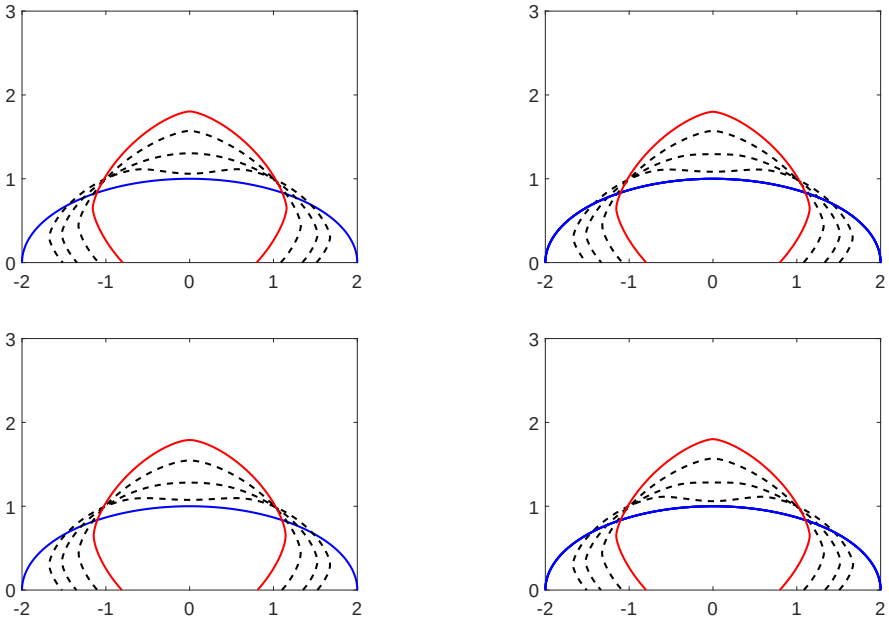

Figure 16: The evolution of SSD with 4-fold anisotropy. Initial curve is the upper half of an ellipse with major axis 4 and minor axis 2. $\beta = 1/17$. Top left: $h = 10^{-2}, \tau = h^2$; Top right: $h = 10^{-2}, \tau^2 = h^2$; Bottom left: $h = 10^{-2}, \tau^3 = h^2$; Bottom right: $h = 1/1600, \tau^4 = h^2$.

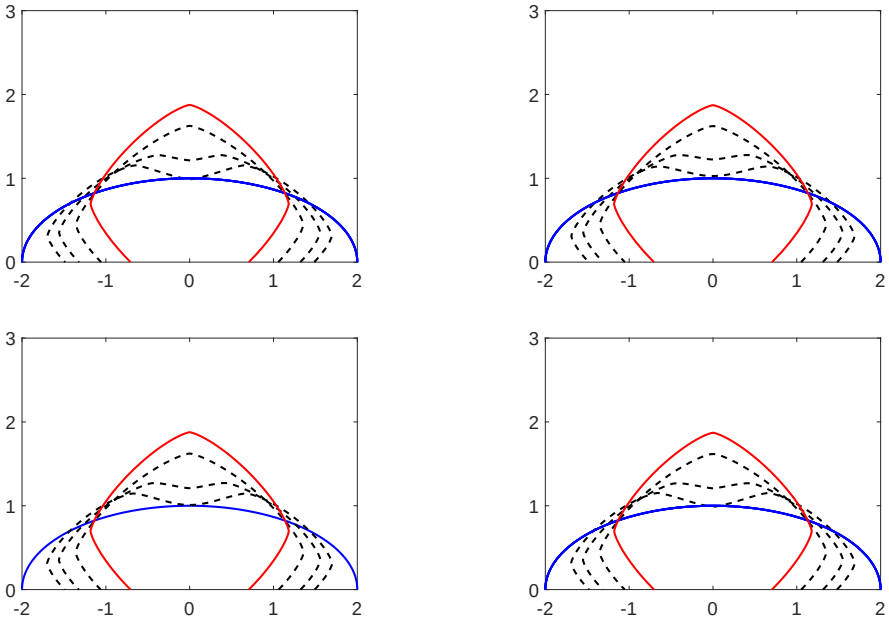

Figure 17: The evolution of SSD with l^4-norm anisotropy. Initial curve is the upper half of an ellipse with major axis 4 and minor axis 2. Top left: $h = 10^{-2}, \tau = h^2$; Top right: $h = 10^{-2}, \tau^2 = h^2$; Bottom left: $h = 10^{-2}, \tau^3 = h^2$; Bottom right: $h = 1/1600, \tau^4 = h^2$.

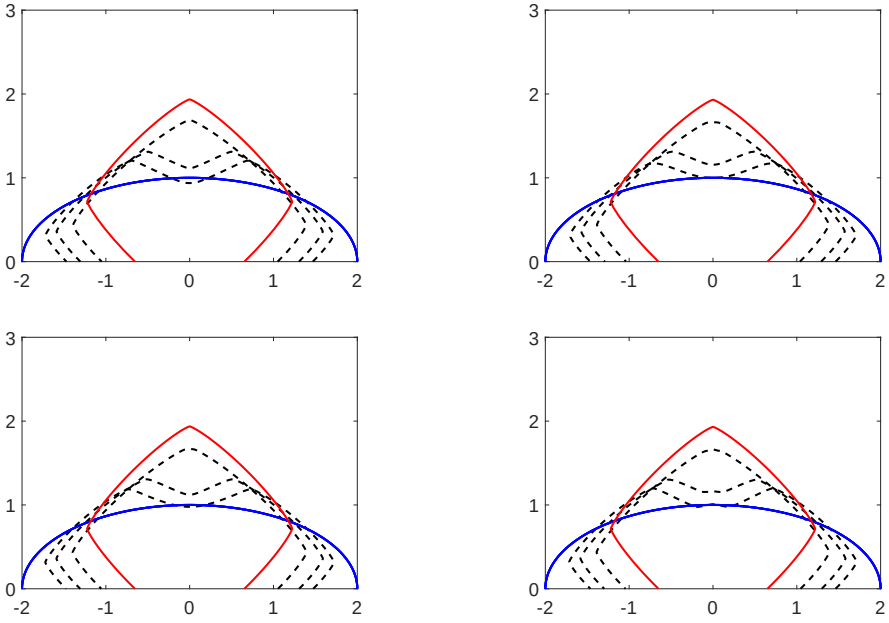

Figure 18: The evolution of SSD with l^6-norm anisotropy. Initial curve is the upper half of an ellipse with major axis 4 and minor axis 2. Top left: $h = 10^{-2}, \tau = h^2$; Top right: $h = 10^{-2}, \tau^2 = h^2$; Bottom left: $h = 10^{-2}, \tau^3 = h^2$; Bottom right: $h = 1/1600, \tau^4 = h^2$.

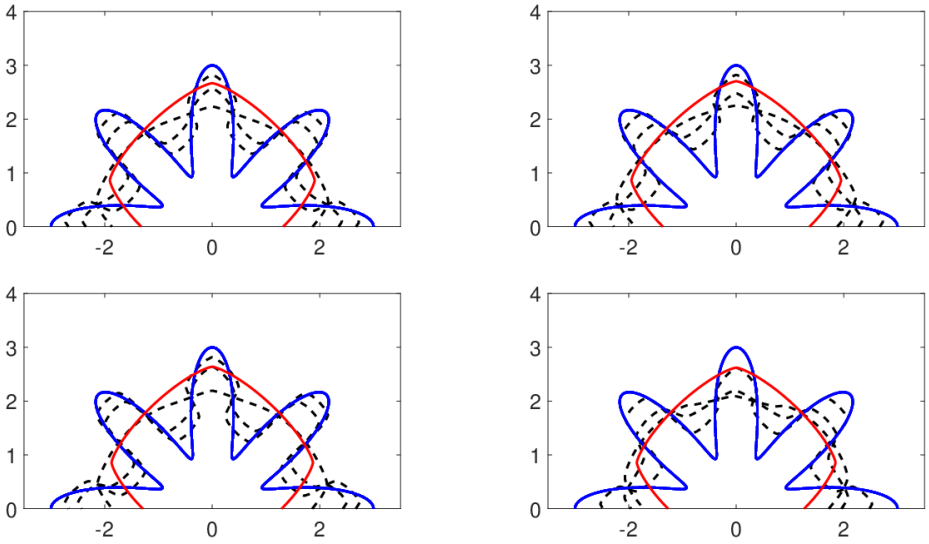

Figure 19: The evolution of SSD with l^4-norm anisotropy. Initial curve is the upper half of a flower, and the parameter equation of this flower is $x=(2+\cos(16\pi\rho))\cos(2\pi\rho), y=(2+\cos(16\pi\rho))\sin(2\pi\rho)$. Top left: $h=1/200, \tau=10^{-3}$; Top right: $h=1/200, \tau=10^{-3}$; Bottom left: $h=1/200, \tau=10^{-3}$; Bottom right: $h=1/200, \tau=4\times10^{-3}$.

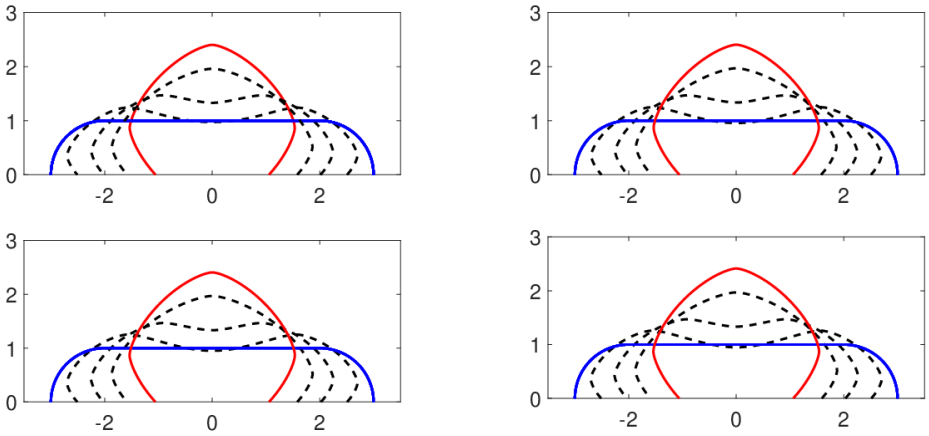

Figure 20: The evolution of SSD with 4-fold anisotropy. The initial curve is the upper half of an ellipse with major axis 4 and minor axis 2, which is divided into two halves and connected by two segments of length 2 in the middle, and $\beta=1/17$. Top left: $h=1/120, \tau=10^{-2}$; Top right: $h=1/120, \tau=10^{-2}$; Bottom left: $h=1/120, \tau=10^{-2}$; Bottom right: $h=1/120, \tau=10^{-2}$.

References

[1] E. Bänsch, P. Morin and R.H. Nochetto, *Surface diffusion of graphs: Variational formulation, error analysis, and simulation*, SIAM J. Numer. Anal. **42**, 773–799 (2004).

[2] W. Bao, W. Jiang and Y. Li, *A symmetrized parametric finite element method for anisotropic surface diffusion of closed curves*, SIAM J. Numer. Anal. **61**, 617–641 (2023).

[3] W. Bao, W. Jiang, Y. Wang and Q. Zhao, *A parametric finite element method for solid-state dewetting problems with anisotropic surface energies*, J. Comput. Phys. **330**, 380–400 (2017).
[4] W. Bao and Y. Li, *A symmetrized parametric finite element method for anisotropic surface diffusion in three dimensions*, SIAM J. Sci. Comput. **45**, A1438–A1461 (2023).
[5] W. Bao and Y. Li, *A structure-preserving parametric finite element method for geometric flows with anisotropic surface energy*, Numer. Math. **156**, 609–639 (2024).
[6] W. Bao and Q. Zhao, *A structure-preserving parametric finite element method for surface diffusion*, SIAM J. Numer. Anal. **59**, 2775–2799 (2021).
[7] W. Bao and Q. Zhao, *An energy-stable parametric finite element method for simulating solid-state dewetting problems in three dimensions*, J. Comput. Math. **41**, 771–796 (2023).
[8] J.W. Barrett, H. Garcke and R. Nürnberg, *On the variational approximation of combined second and fourth order geometric evolution equations*, SIAM J. Sci. Comput. **29**, 1006–1041 (2007).
[9] J.W. Barrett, H. Garcke and R. Nürnberg, *A parametric finite element method for fourth order geometric evolution equations*, J. Comput. Phys. **222**, 441–467 (2007).
[10] J.W. Barrett, H. Garcke and R. Nürnberg, *Numerical approximation of anisotropic geometric evolution equations in the plane*, IMA J. Numer. Anal. **28**, 292–330 (2008).
[11] J.W. Barrett, H. Garcke and R. Nürnberg, *A variational formulation of anisotropic geometric evolution equations in higher dimensions*, Numer. Math. **109**, 1–44 (2008).
[12] J.W. Barrett, H. Garcke and R. Nürnberg, *Finite element methods for fourth order axisymmetric geometric evolution equations*, J. Comput. Phys. **376**, 733–766 (2019).
[13] J.W. Cahn, *Stability, microstructural evolution, grain growth, and coarsening in a two-dimensional two-phase microstructure*, Acta Mater. **39**, 2189–2199 (1991).
[14] J.W. Cahn and J.E. Taylor, *Surface motion by surface diffusion*, Acta Metall. Mater. **42**(4), 1045–1063 (1994).
[15] K. Deckelnick, G. Dziuk and C.M. Elliott, *Computation of geometric partial differential equations and mean curvature flow*, Acta Numer. **14**, 139–232 (2005).
[16] K. Deckelnick, G. Dziuk and C.M. Elliott, *Fully discrete finite element approximation for anisotropic surface diffusion of graphs*, SIAM J. Numer. Anal. **43**, 1112–1138 (2005).
[17] E. Dornel, J.C. Barbe, F. De Crécy, G. Lacolle and J. Eymery, *Surface diffusion dewetting of thin solid films: Numerical method and application to Si/Sio2*, Phys. Rev. B **73**, 115427 (2006).
[18] P. Du, M. Khenner and H. Wong, *A tangent-plane marker-particle method for the computation of three-dimensional solid surfaces evolving by surface diffusion on a substrate*, J. Comput. Phys. **229**, 813–827 (2010).
[19] Q. Du and X. Feng, *The phase field method for geometric moving interfaces and their numerical approximations*, Handb. Numer. Anal. **21**, 425–508 (2020).
[20] B. Duan and B. Li, *New artificial tangential motions for parametric finite element approximation of surface evolution*, SIAM J. Sci. Comput. **46**, A587–A608 (2024).
[21] M. Dziwnik, A. Münch and B. Wagner, *An anisotropic phase-field model for solid-state dewetting and its sharp-interface limit*, Nonlinearity **30**, 1465–1496 (2017).
[22] I. Fonseca, A. Pratelli and B. Zwicknagl, *Shapes of epitaxially grown quantum dots*, Arch. Ration. Mech. Anal. **214**, 359–401 (2014).
[23] D.W. Hoffman and J.W. Cahn, *A vector thermodynamics for anisotropic surfaces: I. Fundamentals and application to plane surface junctions*, Surf. Sci. **31**, 368–388 (1972).
[24] Q.-A. Huang, W. Jiang and J.Z. Yang, *An efficient and unconditionally energy stable scheme for simulating solid-state dewetting of thin films with isotropic surface energy*, Commu. Comput. Phys. **26**, 1444–1470 (2019).
[25] W. Huang, W. Jiang and Q. Zhao, *A θ-l formulation-based finite element method for solving axisymmetric solid-state dewetting problems*, East Asian J. Appl. Math **11**, 389–405 (2021).

[26] W. Jiang, W. Bao, C.V. Thompson and D.J. Srolovitz, *Phase field approach for simulating solid-state dewetting problems*, Acta Mater. **60**, 5578–5592 (2012).
[27] W. Jiang, C. Su and G. Zhang, *Stable backward differentiation formula time discretization of BGN-based parametric finite element methods for geometric flows*, SIAM J. Sci. Comput. **46**, A2874–A2898 (2024).
[28] W. Jiang, Y. Wang, Q. Zhao, D.J. Srolovitz and W. Bao, *Solid-state dewetting and island morphologies in strongly anisotropic materials*, Scr. Mater. **115**, 123–127 (2016).
[29] W. Jiang and Q. Zhao, *Sharp-interface approach for simulating solid-state dewetting in two dimensions: A Cahn-Hoffman ξ-vector formulation*, Physica D **390**, 69–83 (2019).
[30] W. Jiang, Q. Zhao and W. Bao, *Sharp-interface model for simulating solid-state dewetting in three dimensions*, SIAM J. Appl. Math. **80**, 1654–1677 (2020).
[31] E. Jiran and C.V. Thompson, *Capillary instabilities in thin films*, J. Electron. Mater. **19**, 1153–1160 (1990).
[32] E. Jiran and C.V. Thompson, *Capillary instabilities in thin, continuous films*, Thin Solid Films. **208**, 23–28 (1992).
[33] W. Kan and H. Wong, *Fingering instability of a retracting solid film edge*, J. Appl. Phys. **97**, 043515 (2005).
[34] G.H. Kim and C.V. Thompson, *Effect of surface energy anisotropy on Rayleigh-like solid-state dewetting and nanowire stability*, Acta Mater. **84**, 190–201 (2015).
[35] G.H. Kim, R.V. Zucker, J. Ye, W.C. Carter and C.V. Thompson, *Quantitative analysis of anisotropic edge retraction by solid-state dewetting of thin single crystal films*, J. Appl. Phys. **113**, 043512 (2013).
[36] M. Li, Y. Li and L. Pei, *A symmetrized parametric finite element method for simulating solid-state dewetting problems*, Appl. Math. Model. **121**, 731–750 (2023).
[37] M. Li and Q. Zhao, *Parametric finite element approximations for anisotropic surface diffusion with axisymmetric geometry*, J. Comput. Phys. **497**, 112632 (2024).
[38] M. Li and C. Zhou, *Energy-stable parametric finite element approximations for regularized solid-state dewetting problems in strongly anisotropic materials*, J. Nonlinear Sci. **35**, 52 (2025).
[39] M. Li and C. Zhou, *Structure-preserving parametric finite element methods for simulating axisymmetric solid-state dewetting problems with anisotropic surface energies*, J. Comput. Phys. **531**, 113944 (2025).
[40] Y. Li and W. Bao, *An energy-stable parametric finite element method for anisotropic surface diffusion*, J. Comput. Phys. **446**, 110658 (2021).
[41] Z. Li, H. Zhao and H. Gao, *A numerical study of electro-migration voiding by evolving level set functions on a fixed cartesian grid*, J. Comput. Phys. **152**, 281–304 (1999).
[42] W.W. Mullins, *Theory of thermal grooving*, J. Appl. Phys. **28**, 333–339 (1957).
[43] M. Naffouti et al., *Complex dewetting scenarios of ultrathin silicon films for large-scale nanoarchitectures*, Sci. Adv. **3**, eaao1472 (2017).
[44] K. Oura, V.G. Lifshits, A.A. Saranin, A.V. Zotov and M. Katayama, *Surface Science: An Introduction*, Springer Science & Business Media (2013).
[45] C.V. Thompson, *Solid-state dewetting of thin films*, Annu. Rev. Mater. Res. **42**, 399–434 (2012).
[46] Y. Wang, W. Jiang, W. Bao and D.J. Srolovitz, *Sharp interface model for solid-state dewetting problems with weakly anisotropic surface energies*, Phys. Rev. B **91**, 045303 (2015).
[47] A.A. Wheeler, *Cahn-Hoffman ξ-vector and its relation to diffuse interface models of phase transitions*, J. Stat. Phys. **95**, 1245–1280 (1999).
[48] H. Wong, P.W. Voorhees, M.J. Miksis and S.H. Davis, *Periodic mass shedding of a retracting solid film step*, Acta Mater. **48**, 1719–1728 (2000).
[49] Y. Xu and C.-W. Shu, *Local discontinuous Galerkin method for surface diffusion and Willmore*

flow of graphs, J. Sci. Comput **40**, 375–390 (2009).
[50] J. Ye and C.V. Thompson, *Mechanisms of complex morphological evolution during solid-state dewetting of single-crystal nickel thin films*, Appl. Phys. Lett. **97**, 071904 (2010).
[51] J. Ye and C.V. Thompson, *Regular pattern formation through the retraction and pinch-off of edges during solid-state dewetting of patterned single crystal films*, Phys. Rev. B **82**, 193408 (2010).
[52] J. Ye and C.V. Thompson, *Anisotropic edge retraction and hole growth during solid-state dewetting of single crystal nickel thin films*, Acta Mater. **59**, 582–589 (2011).
[53] J. Ye and C.V. Thompson, *Templated solid-state dewetting to controllably produce complex patterns*, Adv. Mater. **23**, 1567–1571 (2011).
[54] Y. Zhang, Y. Li and W. Ying, *A stabilized parametric finite element method for surface diffusion with an arbitrary surface energy*, J. Comput. Phys. **523**, 113605 (2025).
[55] Q. Zhao, *A sharp-interface model and its numerical approximation for solid-state dewetting with axisymmetric geometry*, J. Comput. Appl. Math. **361**, 144–156 (2019).
[56] Q. Zhao, W. Jiang and W. Bao, *A parametric finite element method for solid-state dewetting problems in three dimensions*, SIAM J. Sci. Comput. **42**, B327–B352 (2020).
[57] Q. Zhao, W. Jiang and W. Bao, *An energy-stable parametric finite element method for simulating solid-state dewetting*, IMA J. Numer. Aanl. **41**, 2026–2055 (2021).